CONTROLLING AND MODELLING OF TWIN INDUCED STRAIN LOCALIZATION IN ROLLING OF MAGNESIUM AZ31

A THESIS SUBMITTED TO
THE GRADUATE SCHOOL OF NATURAL AND APPLIED SCIENCES
OF
MIDDLE EAST TECHNICAL UNIVERSITY

BY

KÜBRA ISMAIL

IN PARTIAL FULFILLMENT OF THE REQUIREMENTS
FOR
THE DEGREE OF MASTER OF SCIENCE
IN
METALLURGICAL AND MATERIALS ENGINEERING

SEPTEMBER 2019

Approval of the thesis:

CONTROLLING AND MODELLING OF TWIN INDUCED STRAIN LOCALIZATION IN ROLLING OF MAGNESIUM AZ31

submitted by **KÜBRA ISMAIL** in partial fulfillment of the requirements for the degree of **Master of Science in Metallurgical and Materials Engineering Department, Middle East Technical University** by,

Prof. Dr. Halil Kalıpçılar
Dean, Graduate School of **Natural and Applied Sciences** _____

Prof. Dr. C. Hakan Gür
Head of Department, **Met. and Mat. Eng.** _____

Assist. Prof. Dr. Mert Efe
Supervisor, **Met. and Mat. Eng., METU** _____

Examining Committee Members:

Prof. Dr. Tayfur Öztürk
Met. and Mat. Eng , METU _____

Assist. Prof. Dr. Mert Efe
Met. and Mat. Eng., METU _____

Prof. Dr. Abdullah Öztürk
Met. and Mat. Eng., METU _____

Assoc. Prof. Dr. Caner Şimşir
Met. and Mat. Eng., METU _____

Assist. Prof. Dr. Kemal Davut
Met. and Mat. Eng., ATILIM UNIVERSITY _____

Date: 02.09.2019

I hereby declare that all information in this document has been obtained and presented in accordance with academic rules and ethical conduct. I also declare that, as required by these rules and conduct, I have fully cited and referenced all material and results that are not original to this work.

Name, Surname: Kübra ISMAIL

Signature:

ABSTRACT

CONTROLLING AND MODELLING OF TWIN INDUCED STRAIN LOCALIZATION IN ROLLING OF MAGNESIUM AZ31

ISMAIL, Kübra
Master of Science, Metallurgical and Materials Engineering
Supervisor: Assist. Prof. Dr. Mert Efe

September 2019, 66 pages

Formability of AZ31 Magnesium alloy has certain limits below 200 ℃ and depends strongly on temperature, due to the strain localization and shear banding associated with the twinning activity. In this thesis, magnesium sheets with basal, off-basal (90° tilted) and mixed (50% basal + 50% off-basal) textures are rolled between room temperature and 165 ℃ to understand and control the twinning-induced localizations. By increasing strain from 0.1 to 0.6 and raising the temperature, the fraction of flow localized regions increases and the strain intensity in these regions is controlled by the starting texture. The sheet with basal texture develops the most intense localizations at room temperature and fails by shear banding at only 0.16 strain. Off-basal sheet, on the other hand, has similar fraction of twins and localizations but capable of deforming twice the strain (0.36) without shear banding. Maximum uniform strains increase with temperature and reach to 0.60, 0.50, and 0.33 at 165 ℃ for off-basal, mixed, and basal textures, respectively. When the fraction of strain localized regions and the strain intensity in them are incorporated into a model, it was possible to predict the maximum rolling strain for a given starting texture and temperature.

Keywords: Shear Banding, Localization, Magnesium, Twinning, Texture

ÖZ

MAGNEZYUM AZ31'İN HADDELENMESİNDE OLUŞAN İKİZLENMEDEN KAYNAKLI GERİNİM YERELLEŞMELERİNİN KONTROLÜ VE MODELLENMESİ

ISMAIL, Kübra
Yüksek Lisans, Metalurji ve Malzeme Mühendisliği
Tez Danışmanı: Dr. Öğr. Üyesi Mert Efe

Eylül 2019, 66 sayfa

AZ31 Magnezyum alaşımının 200 ℃ altındaki sıcaklıklarda şekillendirilebilirliği, ikizlenmeden kaynaklı gerinim yerelleşmesi ve kesme kuşakları nedeniyle kısıtlıdır ve sıcaklığa aşırı bağlıdır. Bu tezde, bazal, bazal olmayan (90° dönmüş), ve karışık (50% bazal + 50% bazal olmayan) dokulu magnezyum levhaları, ikizlenmeden kaynaklı yerelleşmeleri anlamak ve kontrol etmek için oda sıcaklığı ile 165 ℃ arasındaki sıcaklıklarda haddelenmiştir. Gerinim 0.1'den 0.6'ya yükselirken ve sıcaklık artarken akışın yerelleştiği bölgelerin oranı artmaktadır ve bu bölgelerdeki gerinim yoğunluğu başlangıç dokusu tarafından kontrol edilmektedir. Bazal dokuya sahip levhada en yoğun yerelleşme oda sıcaklığında oluşmakta ve levha sadece 0.16 gerinimde kesme bandından kırılmaktadır. Öte yandan benzer ikizlenme ve yerelleşme oranına sahip bazal dokulu olmayan levha, iki katı (0.36) gerinime kadar dayanmakta ve kesme bandı gözlemlenmeden deforme olmaktadır. Maksimum eş dağılımlı gerinim sıcaklığa göre artmakta ve 165 ℃'de bazal dokulu olmayan levhalarda 0.6, karışık dokulu levhalarda 0.5 ve bazal dokulu levhalarda 0.33'e ulaşmaktadır. Gerinim yerelleşmesi gösteren bölgelerin oranı ve bu bölgelerdeki gerinim yoğunluğu bir modele koyulduğunda, belirli bir başlangıç dokusu ve sıcaklığındaki maksimum haddeleme gerinimini tahmin etmek mümkün olmuştur.

Anahtar Kelimeler: Kesme bandı, Lokalizasyon, Magnezyum, İkizlenme, Yapı

To my hero, my father

ACKNOWLEDGEMENTS

This work was inpart by TUBITAK project number of 115M642 and supported by European Commission's Research Executive Agency's Marie Skłodowska Curie Actions – Career Integration Grant (FP7-PEOPLE-2013-CIG) with grant agreement #631774.

I would like to express my deep sense of respect and gratitude to Assist. Prof. Dr. Mert Efe for his constructive suggestions and guidance that have enabled me to overcome all the problems and difficulties while carrying out the present work. He stayed along with me and motivated constantly and stimulated me to the fullest extent. I thank to TUBITAK for scholarship that made me feel financially comfortable. I feel fortunate for his support and involvement and this is virtually impossible to express them in words. I also express my gratitude to Dr. Süha Tirkeş for the valuable comments and advices and for continuous support during this study. Thanks for all the time has dedicated for me within his busy schedule and thanks to Welding Technology and Non-Distractive Testing Center (WTNDT) crew for their lovely hospitality. My warmest thanks to my best friends, Burak Büyür, Beril Günay Bağ, Duygu Hökelek and her little baby for their mental and physical support all time. Special thanks to my husband Achmet Ismail for his great support and encouragement during all of the period of this thesis.

Heartfelt thanks to my mother Müveddet Atik and my sister Pınar Karadağ who always concern about my progress and help me in any case. Last but not the least, I thank to my little twin niece, Beren and İnci Karadağ who give indescribable feelings to me. Also special thanks to my elder niece Yağmur Ali.

And i love you my father. I know, you either.

TABLE OF CONTENTS

ABSTRACT v

ÖZ vii

ACKNOWLEDGEMENTS x

TABLE OF CONTENTS xi

LIST OF TABLES xiii

LIST OF FIGURES xiv

1. INTRODUCTION 1

2. LITERATURE REVIEW 7

2.1. Magnesium Alloys 7

2.1.1. Magnesium Alloys and Their Properties 11

2.1.2. AZ31 Magnesium Alloys 13

2.2. Deformation Mechanisms and Formability of Magnesium Alloys 15

2.3. Magnesium Sheet Deformation Processes 25

2.3.1. Rolling 25

2.3.2. Twin Roll Casting 27

2.3.3. Extrusion Machining 28

2.4. Motivation and Aim of Study 30

3. EXPERIMENTAL 33

3.1. Rolling Setup 33

3.2. Temperature Data Logger Setup 35

3.3. Material and Methods 35

4. RESULTS AND DISCUSSION 43

4.1. Shear Banding in Rolling and Its Control 43
4.2. Strain, Temperature and Texture Dependence of the Twinning Activity 46
4.3. Twinning-induced Softening and Its Relation to Shear Banding 50
5. SUMMARY & FUTURE WORKS 55
REFERENCES 57

LIST OF TABLES

TABLES

Table 1.1 Automotive part weight reduction versus low Carbon steel 2
Table 2.1 Letters representing alloying elements of magnesium [55] 9
Table 2.2 Basic temper designation of magnesium alloys [56].....10
Table 2.3 Definition of AZ31B–O designation [51] 11
Table 2.4. Chemical content of AZ31 magnesium alloys [65] 14
Table 2.5 Comparison of mechanical properties of AZ31 and AZ61 mg alloy [68] 14
Table 2.6 Slip systems and their parameters of a typical HCP structure [73].....18
Table 2.7 Calculated Schmid factor values for magnesium [79] 21
Table 2.8 Comparison of sheet deformation processes. 30

LIST OF FIGURES

FIGURES

Figure 1.1 Strength and density of different materials [13]..... 2
Figure 1.2 Applications of magnesium alloys in automotive industry[14] 3
Figure 2.1 3D and 2D views of atomic layers in HCP structure[51]..... 7
Figure 2.2 Unit cell and layer arrangement of HCP structure[51]..... 8
Figure 2.3 Some nonferrous metal alloys and their engineering application [53]..... 9
Figure 2.4 Movement of edge dislocation [51]..... 15
Figure 2.5 Deformation in single crystal [51]..... 17
Figure 2.6 Direction of the slip and twin system of magnesium alloys [78]..... 19
Figure 2.7 Schematic relation of loading axes with (a) slip mechanism (b) twinning mechanism (c) projected location of the relative loading direction on the basal plane [79]..... 20
Figure 2.8 Critical resolved shear stress of AZ 31 magnesium alloy with temperature [27,34]..... 22
Figure 2.9 Representation of rolling process[56] 26
Figure 2.10 Representation of twin roll casting process [93]..... 28
Figure 2.11 Schematic view of extrusion-machining [95] 29
Figure 3.1 OAM CAVALLIN M120..... 33
Figure 3.2 Schematic view of rolling process..... 34
Figure 3.3 Natural Instruments data logger 35
Figure 3.4 Optical views of a) rolled and b) rolled ad annealed and c) EBSD result of rolled and annealed 4 mm thick plate..... 37
Figure 3.5 EBSD orientation maps, the associated pole figures and inverse pole figures from RD-TD planes of a) basal, b) off-basal and c) mixed textured strips before rolling. Optical micrograph (d) shows the nonuniform microstructure of the mixed texture. 38

Figure 3.6 The optical as-received images of the a) 2 mm, b) 6 mm and c) 7 mm samples.....39
Figure 3.7 Demonstration of calculation of the strain-localized fraction by using Adobe Photoshop Software ®.....40
Figure 3.8 Temperature distribution during the rolling experiment with a pre-heating temperature of 150 ℃.....41
Figure 4.1 Maximum rolling strain per pass vs. temperature of basal, mixed and off-basal textured specimens.....44
Figure 4.2 True strain per pass vs. temperature of basal texture specimen.....44
Figure 4.3 Optical microstructures of basal textured strips rolled at 120 ℃ a) $\varepsilon = 0.12$, sound strip (inset) b) $\varepsilon = 0.37$, cracked strip (inset). For the cracked strip, the inset shows a piece of the strip, as in this case edge cracking was severe and shattered the strip into small pieces.....45
Figure 4.4 Optical microstructures of a) basal textured and b) off-basal textured strips rolled at 80 ℃ to 0.22 strain.....46
Figure 4.5 Optical microstructures of basal textured strips rolled at 150 ℃ to a strain of a) 0.09 b) 0.19.....47
Figure 4.6 Optical microstructures of basal textured strips rolled at strain of 0.09 a) at room temperature, b) at 120 ℃.....48
Figure 4.7 Area fraction of the strain-localized regions at various strain and temperatures for a) basal, b) mixed and c) off-basal textured samples.....49
Figure 4.8 EBSD orientation maps of a) basal and b) off-basal textured specimens after rolling. In this case, EBSD maps are from the cross-section of the specimens (TD-ND plane) and the loading direction is shown with respect to the image plane 51
Figure 4.9 Experiment and modeling comparison of the temperature and texture dependence of the maximum rolling strain.....54

CHAPTER 1

INTRODUCTION

Magnesium alloys are very suitable for the designs that require lower weight with higher strength [1–3]. Nearly 910,000 tons of magnesium were produced in 2015 and the production volume is getting higher every year [4]. Compared to steels and aluminum alloys magnesium alloys are lower in density and higher in specific strength (strength-to-weight ratio) [5,6]. Moreover, magnesium has much higher specific elastic modulus and lower density than their alternatives like steel and aluminum alloys Figure 1.1. This makes magnesium alloys a preferable candidate to replace other metals, which have low specific properties in industrial applications [5]. Decreasing the weight of automobile parts leads to lower fuel consumption which is one of the main concerns of automotive industry in last decades. It also reduces emission rates and enhances the performance of the automobiles [7–9]. Another important outcome of reducing weight of automobile parts is lowering production costs [10]. Table 1.1 indicates that using magnesium alloys instead of steel can create 55-60% weight reduction. Considering these reasons, magnesium alloy parts are replacing steel to increase the weight efficiency. First parts to replace with magnesium alloys were the parts that do not carry critical loads. BMW manufactured a composite magnesium alloy engine, the R6 that is the lightest 3.0 liter in-line six-cylinder gasoline engine which is listed one of Ward's 10 best engines in 2006-2007 [11,12]. After the developments made in mechanical properties of magnesium alloys, these alloys have been used in various bodies of automobiles including critical load carrying parts which can be seen in Figure 1.2.

Table 1.1 Automotive part weight reduction versus low Carbon steel

Material	**Weight Reduction vs. Low-Carbon Steel**
High-strength Steel	15-25%
Aluminum Alloys	40-50%
Magnesium Alloys	55-60%

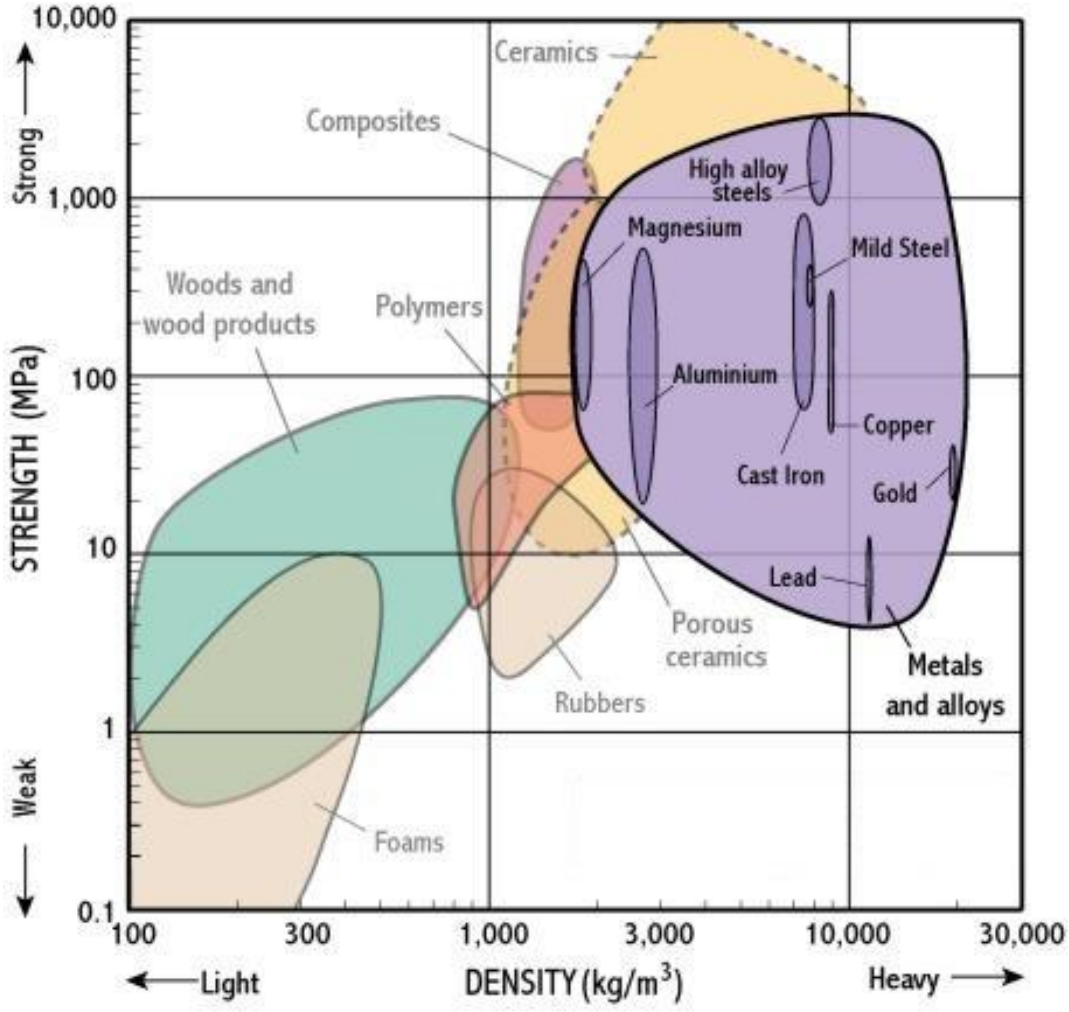

Figure 1.1 Strength and density of different materials [13]

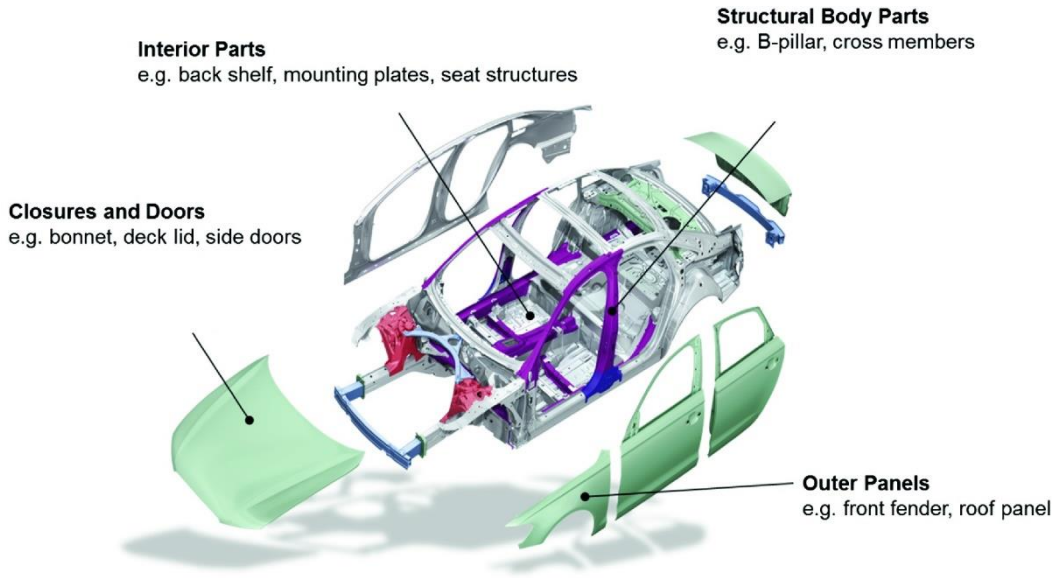

Figure 1.2 Applications of magnesium alloys in automotive industry[14]

Magnesium alloys have widely been used in industrial applications both as semi-finished and final products as cast into the desired net shape or used wrought alloys by applying further shaping processes [15,16]. The most prominent manufacturing techniques for semi-finished magnesium alloys are casting and direct chill casting [17], while rolling [18], twin-roll casting [19–21] and extrusion machining [22] are manufacturing techniques for finished magnesium alloys. Besides, most of the products also require additional forming processes to have desired shape. Wrought alloys that exposed to thermo-mechanical treatment are replacing cast alloys due to their better mechanical properties. Unfortunately, their limited formability is the major barrier to greatly increased magnesium alloy usage [23]. In particular, its extended applications are limited by its low formability at room temperature [24,25]. Then, many manufacturers and scientists have been investigating magnesium deformation mechanisms because of its high strength and low weight being a key issue for many industrial applications. Numerous studies have been performed to understand plastic deformation mechanism and production of magnesium alloys. The

main objective for improvement in the mechanical deformation processing of Mg alloys is understanding the crystallographic slip and twinning behavior.

Mg alloys have a hexagonal-close-packed (hcp) structure, exhibit highly anisotropic mechanical properties, with c/a ratio of 1.624 [26]. The number of independent slip systems for a homogeneous plastic deformation at room temperature is limited because of the symmetry of hexagonal structure. <c+a> dislocation slip and twinning are the main deformation mechanisms to accommodate strain along the c-axis [27]. However, at low temperatures (< 200 ℃) <c+a> dislocation slip is inactive, and the mechanical twinning becomes the only deformation mechanisms when the basal slip is geometrically restricted [28]. Basal slip has almost zero Schmid factor (S) when the deformation is along the c-axis of the strongly textured magnesium. Then, the deformation is possible by $\{10-\bar{1}1\}$ or $\{10-\bar{1}3\}$ contraction twinning modes in compressive-type processes (e.g. rolling), considering the critical resolved shear stress for secondary slip modes are almost 100 times more than that of basal slip at ambient temperatures [29–31].

The origin of flow localizations and cracking at low temperatures has recently been linked to the twinning activity [32,33]. One substantial characteristic of deformation twinning is that grains unfavorably oriented for basal slip can be reoriented into the more appropriate orientations [34]. In other words, the softening effect induced by contraction and double twinning leads to a substantial weakening of the microstructure [27,35]. When twinning happens in the strongly textured magnesium, the initial basal planes tilt by 56° or 64° for contraction {10-11} twins and 38° for double {10-11} {10-12} twins. As the tilted basal planes now favor slip due to non-zero S, the deformation concentrates to the twinned areas leading to the texture softening [36]. The entire deformation localizes into the narrow twins with limited number in the microstructure. With increasing deformation, twinning becomes auto-catalytic [37]. This triggers a network of twins and leads to the formation of sharp, shear bands consisting of many interconnected twins [33,38,39]. The intense strain localization can sometimes cause dynamic recrystallization (DRX) within the bands. As the

deformation temperature increases, DRX grains become more clear and larger, transforming the twinned areas into recrystallized macroscopic bands. In this case, the twins diminish and may not be visible, but the initial twinning activity is still the reason of the twinning-induced recrystallization (TDRX) within the bands [40].

There are several strategies to suppress twinning-induced shear banding in magnesium. Alloying of magnesium with rare-earth elements both weakens the initial basal texture and decreases the CRSS of non-basal slip systems. These allow considerable slip at room temperature instead of twinning [41]. Alternatively, texture and grain size of the sheet can be modified by shear-type deformation methods [42–45]. Tilted-basal textures resulting from shear-type processes encourage basal slip due to non-zero S [46,47]. Fine grain size (< 10 μm) promote non-basal slip at the grain boundaries and contribute to the ductility [48]. Finally, an increase of deformation temperature above 200 ℃ activates non-basal slip system and suppresses the twinning [32,35,49]. Therefore, larger uniform strains with homogenous microstructures become possible in forming of magnesium by controlling the starting texture, grain size, and the deformation temperature.

In this study, magnesium sheets with basal, off-basal (90° tilted), and mixed (50% basal + 50% off-basal) textures are rolled between room temperature and 165 ℃ to understand and control the twinning-induced localizations. The interactive effects of starting texture and temperature are investigated to understand and control the twinning-induced shear banding during rolling. Sheets with three distinct starting textures are rolled to increasing amount of strains per pass until they fail by severe shear banding. Electron Backscatter Diffraction (EBSD) method was used to investigate these highly deformed AZ31 magnesium alloys and their orientation and texture change was identified. The experiments are repeated over a wide range of temperatures to control the extent of twinning and softening. Then, the maximum uniform rolling strains are documented at each combination of texture and temperature. In addition to the experiments, a texture and temperature dependent model is developed for the twinning-induced softening phenomena. The model treats

the magnesium as a composite with soft twinned regions where basal slip is possible, together with hard matrix regions where the basal slip is restricted. The model gives the maximum amount of deformation without shear banding, which results in uniform microstructures and defect-free final products.

CHAPTER 2

LITERATURE REVIEW

2.1. Magnesium Alloys

Magnesium is an alkaline earth metal which is a member of the second group of periodic table with atomic number is 12. Magnesium is one of the lowest-weighted metal, its density 1.77 g/cm^3. Atomic Structure of Magnesium is hexagonal closed packed (HCP) (Figure 2.1) like cadmium, titanium, zirconium and zinc. Packing factor and c/a ratio are two important parameters to define the structure of an HCP metal (Figure 2.2). An ideal HCP structure has maximum packing factor of 0.74 and axial ratio (c/a ratio) of 1.633 These values may differ in other HCP metals. Slip on basal plane becomes the dominant slip mode when the c/a ratio is bigger than ideal ratio. On the other hand, when the c/a ratio is lower than ideal ratio, the prismatic slip becomes more active. Zirconium and titanium alloys are two examples to metals with prismatic slip because of their lower axial ratio. However, magnesium has an exception, it has an axial ratio of 1.624 which is lower than the ideal axial ratio, despite to that basal slip systems are still the dominant slip systems. This is one of the reasons for magnesium to be a brittle metal. It also causes magnesium to have premature failures [50–53].

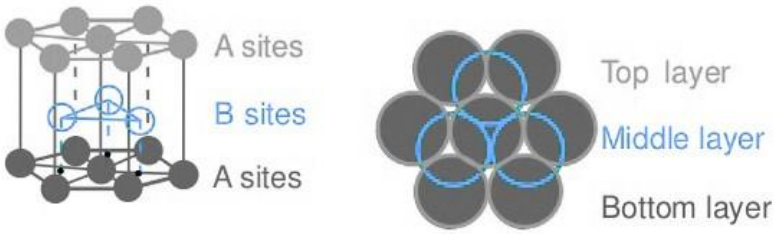

Figure 2.1 3D and 2D views of atomic layers in HCP structure[51]

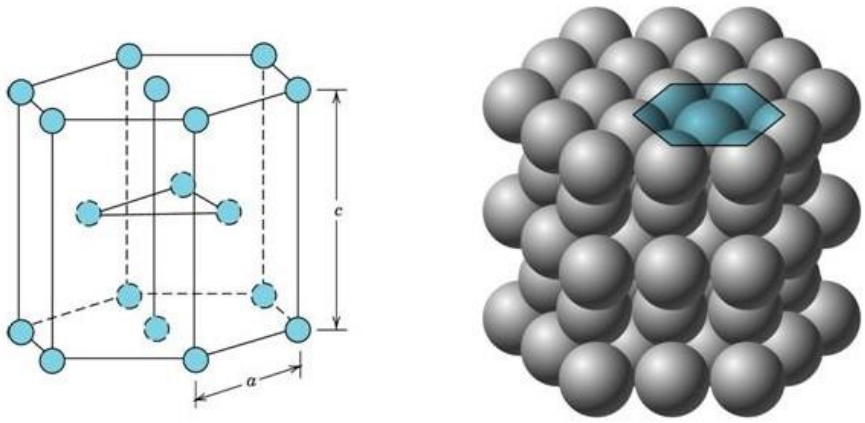

Figure 2.2 Unit cell and layer arrangement of HCP structure[51]

As can be seen in Figure 2.3 magnesium alloy is one of the members of lightweight nonferrous metal alloys like aluminum alloys, beryllium alloys, titanium alloys. Magnesium alloys are the lightest alloys among all these lightweight alloys. This gives us an idea about the great potential of magnesium alloys to be used instead of heavy alloys used in industrial applications. Therefore, disadvantages of magnesium alloys have to be overcome to produce magnesium with demanded quality.

The three of the most important characteristics of magnesium alloys that are lower than the desired quality are;

- corrosion resistance
- strength (relatively)
- formability at room temperature.

New production techniques have been generated in order to get rid of these problems of magnesium alloys and still newer techniques are being studied. Aluminum, zinc, manganese, silicon, copper and some other earth elements are some of the elements that are being mixed with magnesium to have magnesium alloys. Each of alloying elements makes an improvement in different properties. Alloying elements are also used to make magnesium alloys to have better mechanical properties for industrial

production [51,52,54]. The definition of magnesium alloys is done by the abbreviation of these alloying elements, which are represented in Table 2.1. Magnesium alloys are defined by the abbreviation of two main alloying elements and their weight percentage in the alloy. Once the naming of allow is done, also additional letters are used to define standards of composition of alloys, which are as follows;

A First compositions, registered with ASTM

B Second compositions, registered with ASTM

C Third compositions, registered with ASTM

D High purity, registered with ASTM

E High corrosion resistance, registered with ASTM

X Experimental alloy, not registered with ASTM

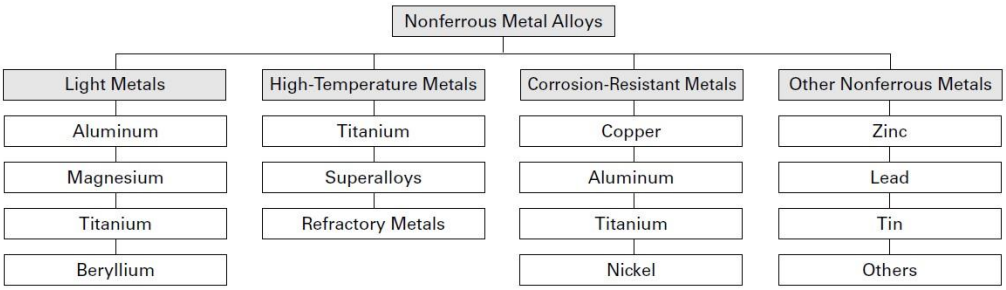

Figure 2.3 Some nonferrous metal alloys and their engineering application [53]

Table 2.1 Letters representing alloying elements of magnesium [55]

Letter	**Alloying Element**	**Letter**	**Alloying Element**
A	Aluminum	N	Nickel
B	Bismuth	P	Lead
C	Copper	Q	Silver
D	Cadmium	R	Chromium
E	Rare Earths	S	Silicon
F	Iron	T	Tin
H	Thorium	V	Gadolinium
J	Strontium	W	Yttrium
K	Zirconium	X	Calcium

L	Lithium	Y	Antimony
M	Manganese	Z	Zinc

Each alloy has different tempering levels that are defined by a capital letter or capital letter and a following number, which can be seen in Table 2.2. To distinguish between tempering levels and alloying element a dash is used. The digit following the designation H1, H2 and H3 shows the final degree of strain-hardening. Tempers between 0 (annealed) and 8 (full hard) are labeled by numbers 1 through 7. Material having a strength about midway between that of the 0 temper and that of the 8 temper is labeled by the number 4 (half hard), between 0 and 4 by the number 2 (quarter hard), between 4 and 8 by the number 6 (three-quarter hard), etc [56].

Table 2.2 Basic temper designation of magnesium alloys [56]

F	As fabricated
O	Annealed, recrystallized (wrought products only)
H	Strain-hardened
Subdivisions of the "H" Tempers:	
H1	Plus one or more digits…. Strain-hardened only
H2	Plus one or more digits…. Strain-hardened and then partially annealed
H3	Plus one or more digits…. Strain-hardened and then stabilized
W	Solution heat-treated, unstable temper
T	Thermal treated to produce stable tempers other than F, O, or H
Subdivisions of the "T" Tempers:	
T1	Cooled and naturally aged
T2	Annealed (cast products only)
T3	Solution heat-treated and then cold worked
T4	Solution heat-treated
T5	Cooled and artificially aged
T6	Solution heat-treated and artificially aged
T7	Solution heat-treated and stabilized
T8	Solution heat-treated, cold worked and then artificially aged
T9	Solution heat-treated, artificially aged and then cold worked
T10	Cooled, artificially aged, and cold worked

The final designation is like: abbreviation of alloying element – code for level of tempering. An example for AZ31B-O is given in Table 2.3.

Table 2.3 Definition of AZ31B–O designation [51]

AZ	Two main alloying elements; A for aluminum and Z for Zinc
31	Weight percentages of alloying element; 3% of aluminum and 1% of Zinc
B	Second compositions, registered with ASTM
O	Annealed, Recrystallized

Magnesium alloys can be produced in too many different ways. However, die casting, DC casting, hot or cold rolling, twin roll casting and extrusion machining are most common ways to produce magnesium alloys. Magnesium alloys are mostly used in the as cast form. Alloying is done during casting process and then the alloy is poured into a mold. Machining is the last process to give the final shape of product. Usage of wrought magnesium alloys has recently increased with the help of new production techniques [57–59].

2.1.1. Magnesium Alloys and Their Properties

By addition of alloying elements like Aluminum, Zinc and other elements poor properties of magnesium mentioned above can be altered remarkably. The properties of magnesium alloys boost after adding these elements and that makes magnesium alloys ideal for structural applications, especially where the strength to weight ratio is utmost important. In this section, the effects of addition of some commonly used alloying elements to pure magnesium are discussed. Also changes in mechanical properties of magnesium alloy with increasing the percentages of alloying elements are examined [60,61]. Aluminum and Zinc are two main alloying elements for magnesium; however, there are other elements that are used to make magnesium alloys which are also mentioned below.

Aluminum:

Aluminum is the most common alloying element to the magnesium alloys as it causes the most beneficial effect. The hardness and strength of magnesium alloys is increased by addition of aluminum. By adding aluminum, magnesium alloy becomes easy to cast and solidification range of the alloy is extended. Aluminum addition of more than of 6 wt.% improves the heat treatability of the magnesium alloy; despite the fact that an addition of less than 6 wt.% makes the alloy more suitable for structural applications by enhancing strength and ductility [62].

Zinc:

Zinc is secondly most used alloying element for magnesium after aluminum. In order to increase strength of magnesium alloy in the room temperature zinc is added in with combination with aluminum. However, there is a drawback of addition of zinc which is hot shortness during casting that happens addition of zinc more than 1 wt.% when Al is already present to about 6-7 wt.% in the alloy. Moreover, zinc improves the corrosion resistance of Mg alloys by decreasing the detrimental effects of impurities like iron and nickel which may cause to corrosion. In order to improve strength of the magnesium alloy zinc can also be added as mixture of other alloying elements like thorium, zirconium and rare earth metals [63].

Silicon:

Silicon is a very beneficial alloying element for the magnesium alloys. By forming Mg_2Si particles that embedded to the grain boundaries, silicon improves the fluidity of molten magnesium and also increase the creep resistance of the magnesium alloys. Using silicon as an alloying element may cause some unwanted results if it used in excess amounts. However, if the usage of silicon controlled carefully it can improve corrosion resistance of the alloy and creates better cast ability [62].

Manganese:

Manganese is generally used with iron and heavy earth metals in order to increase the corrosion resistance of the alloy. In magnesium alloys, manganese is used for applications where the salt water is considered. However, manganese has low solid solution solubility especially when mixed with aluminum solubility of manganese decreases to 0.3 wt.%. There is no other considerable benefit of alloying manganese with magnesium [62].

Silver:

Silver increases the mechanical properties of magnesium alloys as it enhances the age hardenability of the alloy [62].

Rare earth elements:

Adding rare earth elements to magnesium alloys considerably increases the strength and hardness of the alloy at high temperatures by forming different precipitates [62].

2.1.2. AZ31 Magnesium Alloys

AZ31 is a magnesium-aluminum-zinc alloy. The exact chemical content of AZ31 magnesium alloys and weight percentages of these contents are given in Table 2.4. AZ31 magnesium alloys are single-phased magnesium alloy. AZ31 magnesium alloys are the lowest aluminum content AZ magnesium alloys. AZ61 and AZ91 have higher aluminum content which are also being used commonly in commercial applications. However, over a wide range temperature, AZ magnesium alloys that have higher aluminum content can easily be precipitated.

Having limited amount of secondary phase makes AZ31 magnesium alloys age hardenable [64]. During precipitation hardening of AZ31 alloy, $Mg_{17}Al_{12}$ phase precipitations are formed.

Table 2.4. Chemical content of AZ31 magnesium alloys [65]

Element	**Content (%)**
Magnesium, Mg	97
Aluminum, Al	2.50 - 3.50
Zinc, Zn	0.60 - 1.40
Manganese, Mn	0.20
Silicon, Si	0.10
Copper, Cu	0.050
Calcium, Ca	0.040
Iron, Fe	0.0050
Nickel, Ni	0.0050

In Table 2.5 mechanical properties of AZ31 and AZ61 alloys are given. Mechanical characteristics of AZ31 magnesium alloys can be summed up as follows;

- They have relatively good machinability. Besides, all magnesium alloys have always a risk of inflammation so that the precautions should be considered.
- They can be welded with arc-welding techniques.
- Stress relieving and full annealing are applicable to the AZ31 magnesium alloys [66,67]

Table 2.5 Comparison of mechanical properties of AZ31 and AZ61 mg alloy [68]

Properties	**AZ31**	**AZ61**
Tensile strength	260 MPa	310 MPa
Yield strength (strain 0.200%)	200 MPa	230 MPa
Compressive yield strength (at 0.2% offset)	97 MPa	130 MPa
Ultimate bearing strength	385 MPa	470 MPa
Bearing yield strength	230 MPa	285 MPa
Shear strength	130 MPa	140 MPa
Shear modulus	17 GPa	17 GPa
Elastic modulus	44.8 GPa	44.8 GPa

Poisson's ratio	0.35	0.35
Elongation at break (in 50 mm)	15%	16%
Hardness, Brinell (500 kg load, 10 mm ball)	49	60
Charpy impact (V-notch)	4.30 J	4.10 J

2.2. Deformation Mechanisms and Formability of Magnesium Alloys

In this section crystallographic properties of hexagonal closed-packed (hcp) metals that mentioned above and deformation mechanisms and formability of magnesium alloys are discussed. Two main deformation mechanisms of Mg alloys are dislocation slip and twinning. This section then indicates the basic concepts of dislocation slip, twinning and the microstructure response to the deformation in the nucleation and growth mechanisms of twinning.

Slip can be considered as dislocation movement of blocks of crystal along certain crystallographic planes (slip planes) as can be seen in Figure 2.4. Slip occurs by means of applied stresses to the system. These applied stresses distort the atomic arrangement and it causes plastic deformation when stress value reaches to critical resolved shear stress in certain slip system. This phenomenon is called slip deformation [51].

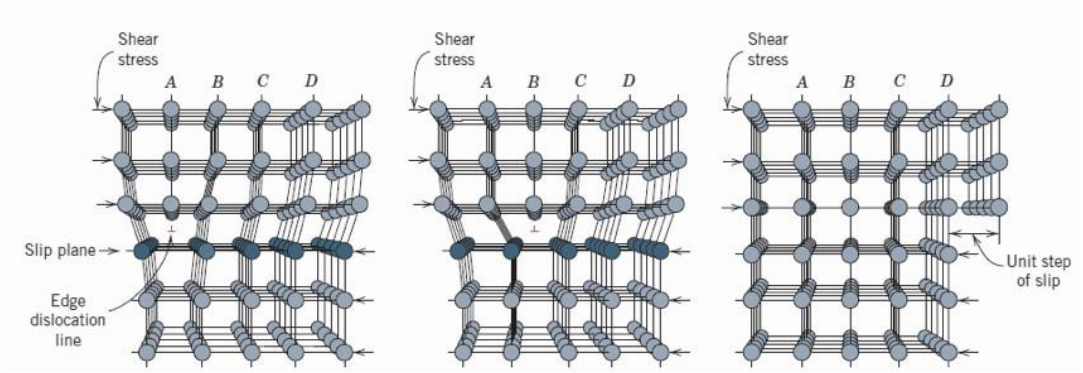

Figure 2.4 Movement of edge dislocation [51]

Slip system can be defined as movement of dislocations along a slip direction on a slip plane. Every crystal structure has different slip systems. For example, FCC crystal

structures have 12 slip systems in room temperature, that makes them highly ductile metals. However, at temperatures lower than room temperature the number of active slip systems of BCC and HCP crystal structure, high loading rate also decreases slip systems of BCC and HCP crystal structure which cause these materials to become brittle under those conditions where only few operational slip systems are available.

Twin formation begins at that stage which happens because of lack of active slip systems. In order to decrease the internal energy, twins form. It can be said that, decrease in the slip systems will result formation of mechanical twinning. Compared to slip mechanism effect of twins to overall deformation is much smaller, however twinning may cause a new crystal orientation. Slipping can be beneficial at this newly formed orientation [51,69]. Geometrical factor and material factor are two main aspects that control the slip deformation. Resolves shear stress determines the geometrical factor while critical resolved shear stress determining the material factor.

Resolved shear stress depends on two parameters, first one is orientation of slip system and the second one is applied stresses. The formula of resolved shear stress for single crystal is:

$$\tau_R = \frac{F}{A}(cos\phi cos\lambda) \quad (1)$$

where F is the applied force,

A is the cross-sectional area,

n is the slip plane normal,

ϕ is the angle between stress direction and slip plane normal and

λ is the angle between stress direction and slip direction.

As shown in Figure 2.5;

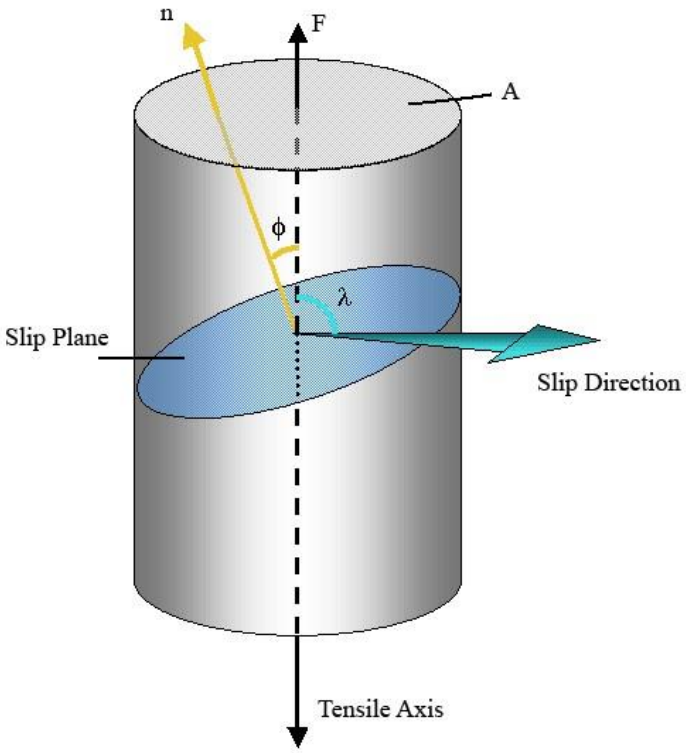

Figure 2.5 Deformation in single crystal [51]

It is found that the value of τ_R reaches at a critical constant value which slip occurs in a given material with specified dislocation density , known as the critical resolved shear stress, τ_C;

$$\tau_C = \sigma(cos\phi cos\lambda)_{max} \quad (2)$$

This is Schmid's Law. The quantity $cos\phi cos\lambda$ is called the Schmid factor. The tensile stress at which the crystal starts to slip is known as the yield stress, σ_Y.

Symbolically, therefore, Schmid's Law can be written:

$$\tau_C = \sigma_Y(cos\phi cos\lambda) \quad (3)$$

Even if there are many slip systems, according to Schmid's Law, the slip system which has the largest resolved shear stress will become active. When resolved shear stress of

that specific system reaches the critical resolved shear stress, deformation will start. Because of that, maximizing the Schmid factor is important. Schmid factor can be calculated for different crystallographic orientations and different loading conditions. It can also be calculated in polycrystalline materials. However, texture of materials which is the combination of direction of grains and distribution these directions has to be known [70]. To sum up, whenever loading direction and slip direction are known, Schmid factor can be calculated.

Two main deformation mechanism of magnesium alloys are slip deformation and twinning. Contraction and tension twinning are two main twin systems and basal slip, prismatic slip and pyramidal slip are three main slip systems [71,72]. The Table 2.6 below shows slip mode, slip plane, slip direction, corresponding burger vector and the number of independent slip systems for all three slip systems.

Table 2.6 Slip systems and their parameters of a typical HCP structure [73]

Slip System	Slip Mode	Slip Plane	Slip Direction	Burger Vector	# of independent slip systems
Basal Slip	$\{0001\}\langle 11\bar{2}0\rangle$	$\{0001\}$	$\langle 11\bar{2}0\rangle$	$^{a}/_{3}\langle 11\bar{2}0\rangle$	3
Prismatic Slip	$\{10\bar{1}0\}\langle 1\bar{2}10\rangle$	$\{10\bar{1}0\}$	$\langle 1\bar{2}10\rangle$	$^{a}/_{3}\langle 11\bar{2}0\rangle$	3
First order Pyramidal Slip	$\{10\bar{1}1\}\langle 1\bar{2}10\rangle$	$\{10\bar{1}1\}$	$\langle 1\bar{2}10\rangle$	$^{a}/_{3}\langle 11\bar{2}0\rangle$	6
Second order Pyramidal Slip	$\{10\bar{1}1\}\langle 11\bar{2}\bar{3}\rangle$	$\{10\bar{1}1\}$	$\langle 11\bar{2}\bar{3}\rangle$	$^{a}/_{3}\langle 11\bar{2}0\rangle$	12

The straining types along the c-axis of HCP of magnesium is defined by tension and contraction twin. Tension twins create an extension along c-axis while contraction twins create contraction along c-axis. TT_1 (tension twin 1) and TT_2 (tension twin 2) are the types of the tension twin system. TT_1 twin occurs on $\{10\bar{1}2\}$ plane with the

burger vector is $a\langle 10\bar{1}1\rangle$. The misorientation angle of TT_1 tension twin between $\langle 11\bar{2}0\rangle$ direction is 86.3°. TT_2 twin occurs on $\{11\bar{2}1\}$ plane with the burger vector is $^{a}/_{3}\langle 11\bar{2}6\rangle$. The misorientation angle of TT_2 tension twin between $\langle 11\bar{2}0\rangle$ direction is 34.8°. CT_1 (contraction twin 1) and CT_2 (contraction twin 2) are the types of contraction twin system. CT_1 twin occurs on $\{10\bar{1}1\}$ plane with the burger vector is $a\langle 10\bar{1}2\rangle$. The misorientation angle of CT_1 tension twin between $\langle 11\bar{2}0\rangle$ direction is 56.2°. CT_2 twin occurs on $\{11\bar{2}2\}$ plane with the burger vector is $^{a}/_{3}\langle 11\bar{2}3\rangle$. The misorientation angle of CT_2 tension twin between $\langle 11\bar{2}0\rangle$ direction is 64.3° [74–77]. The schematic drawings of slip and twin systems are given in Figure 2.6.

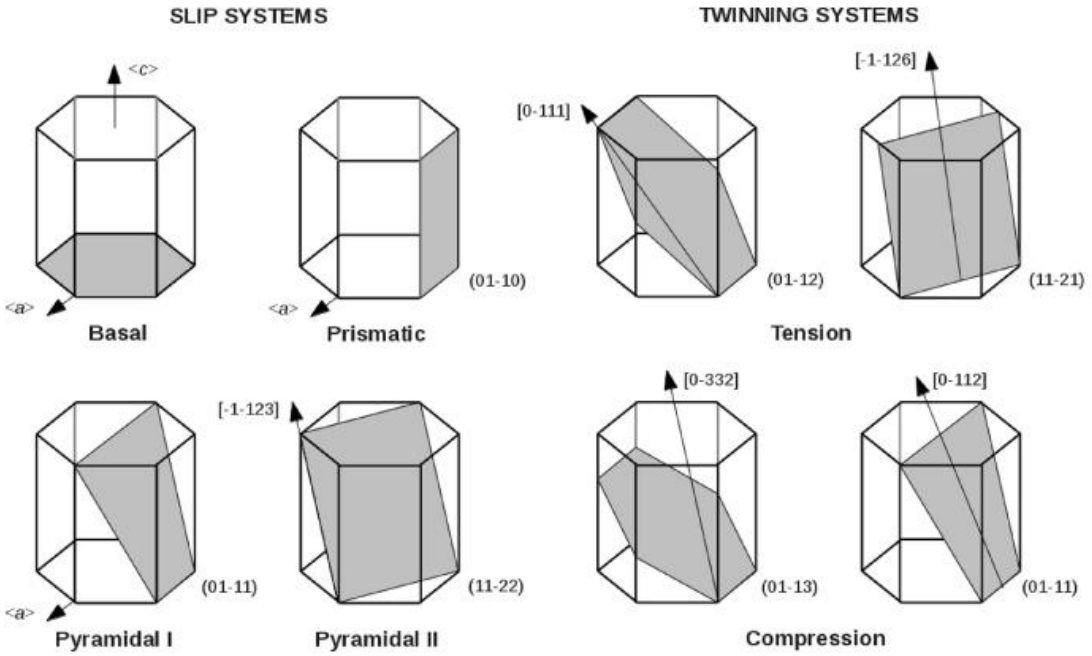

Figure 2.6 Direction of the slip and twin system of magnesium alloys [78]

Schmid factor is very crucial parameter for deformation, it varies with direction and deformation mechanism. When the Schmid factor value increases the resolved shear

stresses also increase. In other words, presence of the deformation mechanism with high Schmid factor depends on the loading conditions.

Figure 2.7 can help in order to have a better understanding of the importance of the loading conditions on deformation mechanisms. Figure 2.7 demonstrates relation between deformation systems and loading axes where loading direction are along $\sigma_1 = 0°,\ \sigma_2 = 15°$ and $\sigma_3 = 30°$ projected location of relative loading direction on basal plane. To illustrate, when the tension load is applied parallel to the c axis, tension twins have higher Schmid factor which makes them dominant deformation mechanism. On the other hand, when the applied load is perpendicular to the c axis, the contraction twins and prismatic slips become dominant deformation mechanism. Moreover, the basal slips become active at where the loading is applied 45° angle with the c axis. These different loading conditions can lead the formability change in the magnesium alloys [79].

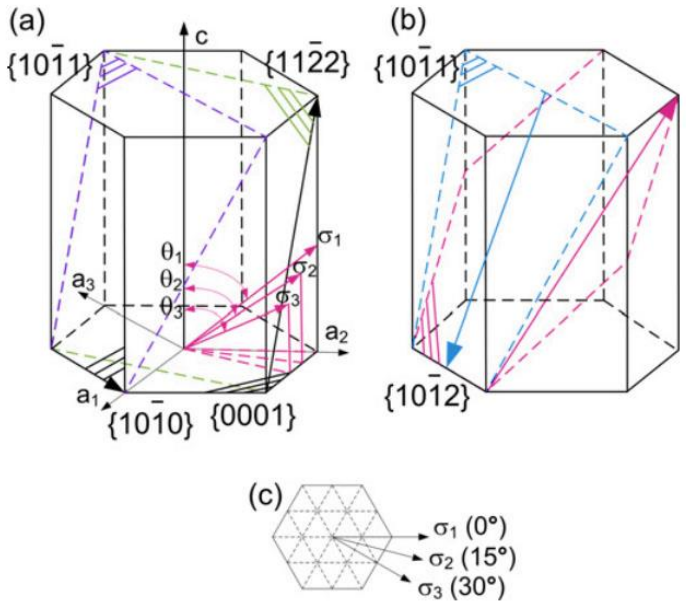

Figure 2.7 Schematic relation of loading axes with (a) slip mechanism (b) twinning mechanism (c) projected location of the relative loading direction on the basal plane [79]

Then, calculated Schmid factor values for magnesium can be seen in Table 2.7.

Table 2.7 Calculated Schmid factor values for magnesium [79]

θ (°)	Basal ⟨**a**⟩			Prismatic ⟨**a**⟩			Pyramidal ⟨**a**⟩		
	σ_1	σ_2	σ_3	σ_1	σ_2	σ_3	σ_1	σ_2	σ_3
0	0	0	0	0	0	0	0	0	0
5	0.087	0.083	0.075	0.003	0.004	0.003	0.041	0.041	0.383
10	0.171	0.165	0.148	0.013	0.015	0.013	0.080	0.084	0.081
20	0.322	0.311	0.278	0.051	0.058	0.051	0.151	0.172	0.175
30	0.433	0.418	0.375	0.108	0.125	0.108	0.204	0.254	0.272
40	0.492	0.475	0.426	0.179	0.207	0.179	0.274	0.346	0.358
45	**0.5***	**0.483***	**0.433***	0.217	0.250	0.217	0.309	0.387	0.395
50	0.492	0.475	0.426	0.254	0.293	0.254	0.340	0.423	0.425
60	0.433	0.418	0.375	0.325	0.375	0.325	0.388	0.475	0.463
70	0.322	0.311	0.278	0.382	0.442	0.382	**0.413***	**0.497***	**0.468***
80	0.171	0.165	0.148	0.420	0.485	0.420	0.411	0.485	0.440
85	0.087	0.083	0.075	0.430	0.496	0.430	0.400	0.466	0.414
90	0	0	0	**0.433***	**0.5***	**0.433***	0.382	0.441	0.382

θ (°)	Pyramidal ⟨**c** + **a**⟩			Extension twinning			Contraction twinning		
	σ_1	σ_2	σ_3	σ_1	σ_2	σ_3	σ_1	σ_2	σ_3
0	0.447	0.447	0.447	**0.499***	**0.499***	**0.499***			
5	0.479	0.478	0.474	0.495	0.497	0.497			
10	**0.497***	**0.495***	**0.490***	0.484	0.486	0.486			
20	0.487	0.485	0.480	0.441	0.442	0.436			
30	0.418	0.419	0.420	0.374	0.373	0.357		0.019	0.034
40	0.327	0.327	0.316	0.293	0.287	0.257	0.122	0.181	0.202
45	0.280	0.271	0.251	0.249	0.241	0.203	0.189	0.255	0.278
50	0.300	0.274	0.204	0.206	0.195	0.149	0.249	0.321	0.346
60	0.418	0.389	0.308	0.125	0.107	0.045	0.339	0.420	0.449
70	0.487	0.455	0.369	0.058	0.034		**0.382***	**0.467***	**0.497***
80	**0.497***	**0.465***	**0.378***	0.015			0.372	0.455	0.485
85	0.479	0.448	0.363	0.004			0.348	0.428	0.457
90	0.447	0.417	0.335	0			0.311	0.387	0.415

θ is the angle between c-axis and loading direction and as can be seen from Table 2.7, during the c-axis deformation θ is 0°, pyramidal $\langle c + a \rangle$ and extension twinning show high values while the maximum values for basal $\langle a \rangle$ slip on loading from three directions are seen when θ is 45°.

Another important factor on deformation mechanisms is the critical resolved shear stress (CRSS) that depends on temperature, slip and twin conditions. Figure 2.8 shows the great temperature dependency of prismatic and pyramidal slips on CRSS. CRSS values of non-basal slips are much higher than basal slip. Having the lowest CRSS value makes the basal slip the major deformation mechanism of magnesium alloys. Due to low CRSS value, basal slip is easy glide deformation mechanism especially at room temperature, which is approximately 0.5 MPa.

However, it can be seen that CRSS values of twins are not considerably affected by the temperature change. Prismatic slip and tension twinning are secondary deformation mode after basal slip at lower temperatures < 200 ℃ (473.15 K) as shown on the Figure 2.8. Moreover, owing to having 10 times lower CRSS value than prismatic slip, tension twinning is more likely to be secondary deformation mode [80,81]. To sum up, in order CRSS to play active role in deformation mechanism, it has to be equal or lower than the resolved shear stress value at the given temperature and Schmid factor has to be high for a given loading condition and texture.

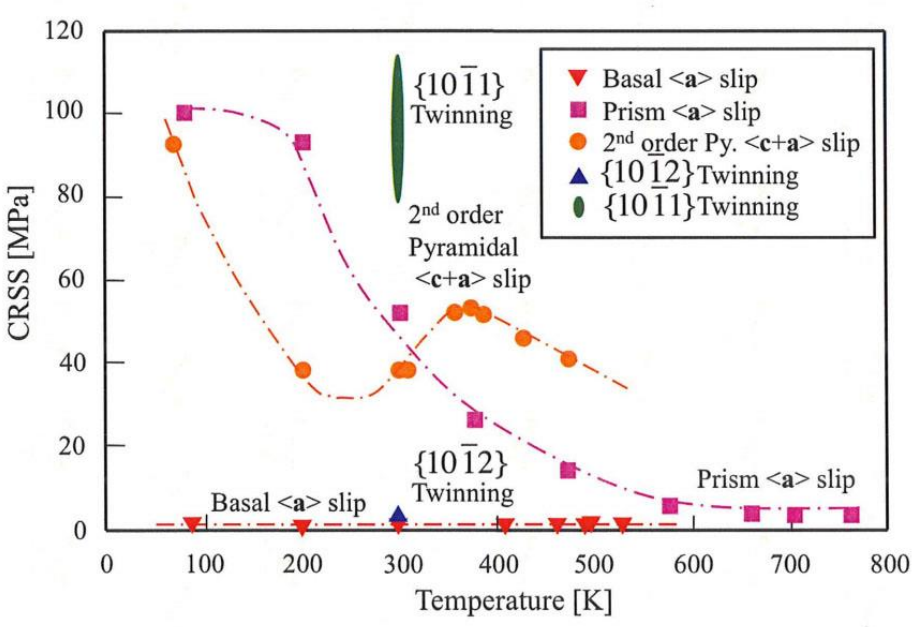

Figure 2.8 Critical resolved shear stress of AZ 31 magnesium alloy with temperature [27,34]

Taylor Criteria propose that in order to get ductile and homogenous plastic deformation polycrystalline materials are required to have a minimum of five active slip systems [82]. However, magnesium alloys do not follow the Taylor Criteria since magnesium alloys have poor formability at room temperatures owing to their two independent activated basal slip modes [83]. At relatively higher than room temperatures, non-basal slip systems are activated. Therefore, prismatic or pyramidal slip systems have two more independent slip modes different than basal slip modes, these magnesium alloys obey the Taylor Criteria [84].

Magnesium alloys lack formability and they also show non-uniform plastic deformation behavior at room temperature due to their limited independent slip modes and not able to perform the Taylor Criteria. However, since at relatively high temperatures (over 180 ℃) non-basal slip modes are activated, an advancement in formability of magnesium alloy can be achieved at elevated temperatures according to the studies about single crystal magnesium [84].

The recent findings show that if activation of non-basal slips at room temperature is possible in any way, the formability of magnesium alloys may be enhanced. These findings state that, both edge and screw dislocation can be acting along $\langle c \rangle$ and $\langle a \rangle$ direction and the single crystal material is loaded compressively given along c-axis. By the help of this way, extra independent slip modes may be activated [85]. Since pyramidal slip modes can perform adequate independent slip modes corresponded by Taylor Criteria if pyramidal slip system ($\langle c + a \rangle$ direction) is activated, the formability behavior of magnesium may be improved.

Addition of some alloying elements to magnesium alloys is a possible way to enhance the formability of magnesium alloy. To alter the current basal texture of basal textured magnesium alloys, particularly rare earth elements are added as further alloying elements. Almost all of the magnesium sheets have a strong basal texture due to deformed by compression loads and further forming processes are applied by load perpendicular to c-axis. By changing basal texture of magnesium alloy, another slip

mode can be also easily activated. Then an improvement of the formability of magnesium can be provided. The effects of three different starting textures on deformability of rolled magnesium sheets at 100 ℃ was studied. It is observed that by activation of non-basal slip planes low temperature ductility has improved [86].

The other important parameter that affects the formability of magnesium alloy at room temperatures is initial grain size. Magnesium alloys with finer grain sizes are more likely to have ductile deformation. Grain refinement is a very effective way to create finer grain sizes in magnesium alloys. Hot rolling is one of the thermo mechanical process techniques that successfully refine the grain size based on dynamic recrystallization behavior. It is stated that, Kim et al. by asymmetric rolling AZ31 magnesium alloy sheets with a fine grain size 1.4 μm and its maximum elongation can be increased up to 35% [87].

Strain rate is another controlling parameter to improve ductility of magnesium alloys. At the high strain rates, ductility of the magnesium alloys decreases. Since there is no time for slip systems to be activated, twinning and shear band deformation becomes prominent.

Another way to increase the formability of magnesium alloy is twinning. When the crystal material loaded along c-axis tension twins become very active due to propensity of magnesium to mechanical twin under applied c-axis load. For magnesium alloy, creating mechanical twinning along c-axis is more preferable than activating non-basal slip systems that helps them to obey Taylor Criteria. The only way to create these mechanical twinning is pure shear stress. However, in order to have shear stress state, there should be a large external stress applied to materials that may cause an abrupt fracture in magnesium alloys [30,88].

Yet, temperature, initial texture, and mechanical twinning can directly change the formability behavior and deformation mechanisms of magnesium alloys. At relatively low temperature due to lack of number of independent slip systems, formability of magnesium alloy is limited by only basal slip not prismatic or pyramidal. Also, if

texture is altered from basal to weak basal in any way, the formability of magnesium alloys would be increased. Moreover, the basal slip will be geometrically limited under loads perpendicular to the c-axis. Then, mechanical twinning formed through shear stress grows into a possible deformation mode for magnesium alloys that plays a huge role of deformation [79]. In some studies, it is said that grain size affects favorably fractions of twinning on the magnesium alloys, but there is no strong evidence grain size to affect slipping behaviors of magnesium alloys [89]. It is stated that, Qizo et al. pre-compressed magnesium alloy strips show enhanced deformation behavior than ones without secondary twinning [90].

To conclude, temperature, initial texture, and strain rate are three major variables that affects the formability of magnesium alloys. The ways to enhance the limited formability of magnesium alloys at low temperatures will be examined further sections.

In this section, magnesium alloy deformation mechanisms and the formability of magnesium alloys were discussed. Magnesium sheet deformation is the main subject of the thesis and will be explained in following sections in detail.

2.3. Magnesium Sheet Deformation Processes

In this section three main deformation processes of magnesium sheet are stated which are rolling, twin roll casting and extrusion machining.

2.3.1. Rolling

As the first commercially available magnesium sheet deformation process, rolling is most widely used forming process which provides high production and close to final product.

Conventional Mg alloys rolling techniques usually resort to multi-pass rolling with a 2-3% reduction per pass at room temperature. Rolling is beneficial technique to achieve a uniform deformation, homogeneous grain structure and strong texture. In contrast, a single-pass large-reduction rolling process results in uneven deformation,

and thus has a probability to achieve bimodal or multimodal grain structures and weakened texture. However, due to the extremely large shear forces in the rolling direction (RD), Mg alloy sheets are very prone to cracking, and thus this rolling technique can hardly be used for production.

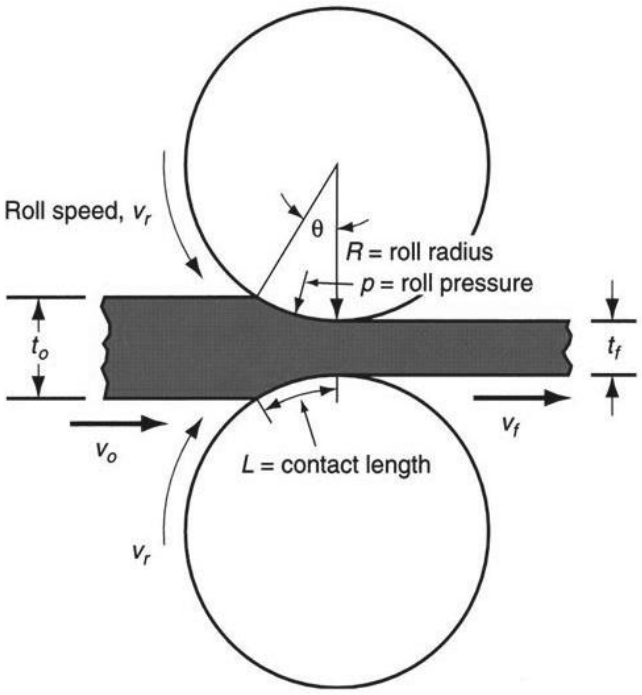

Figure 2.9 Representation of rolling process [56]

A schematic view of rolling is given above in Figure 2.9 where;

t_0 = Initial thickness

t_f = Final thickness

v_0 = Initial velocity of rolling sheet

v_f = Final velocity of rolling sheet

There are two types of rolling that are cold and hot rolling. The former results in sheets having poor formability and high anisotropy at room temperature due to lack of

independent slip systems. It causes edge cracks when over 10% rolling reduction is applied [91]. The latter process activates five more slip systems that greatly improve deformability of magnesium sheets. At high temperatures dynamic recrystallization also helps to increase ductility of magnesium sheets without severe plastic deformation [92].

To conclude, as a sheet deformation process rolling is not beneficial process because it needs to multi-step deformation especially at low temperatures. In order to deform the strip to desired thickness a repeated heat treatment and rolling processes should be done successively. This means, the cost of this processes is relatively high.

2.3.2. Twin Roll Casting

The second common magnesium sheet deformation process is twin roll casting. It has a considerable potential for industrial applications since it facilitates size of the manufacturing of magnesium sheets in an economical way. Twin roll casting is more cost and energy efficient type of production of magnesium sheets because of diminishing of the production steps as to the conventional sheet productions.

On the other hand, this forming process promotes the production of strips with enhanced microstructural properties like lowered segregation, improved inclusion size and refined microstructural homogeneity. Twin roll casting is a combination of casting and hot rolling in one process. The simple schematic of the twin roll casting process is shown on Figure 2.10. Figure 2.10 belongs the process in a horizontal orientation. By a pumping system, molten metal is transferred from furnace to a head box. The head box is connected to a nozzle with a level of height above nozzle entry in order to feed molten metal by the help of the gravitational force. Then molten metal is fed into the gap between two counter rotating rolls and the roll surfaces play a role in a mold for the molten metal to transfer the heat and the solidification starts at the beginning of the contact region between the melt and roll surfaces. Right after the solidification of the magnesium alloy, the solid material is hot rolled while pulling inside the roll entrance region by the rotating rolls [93].

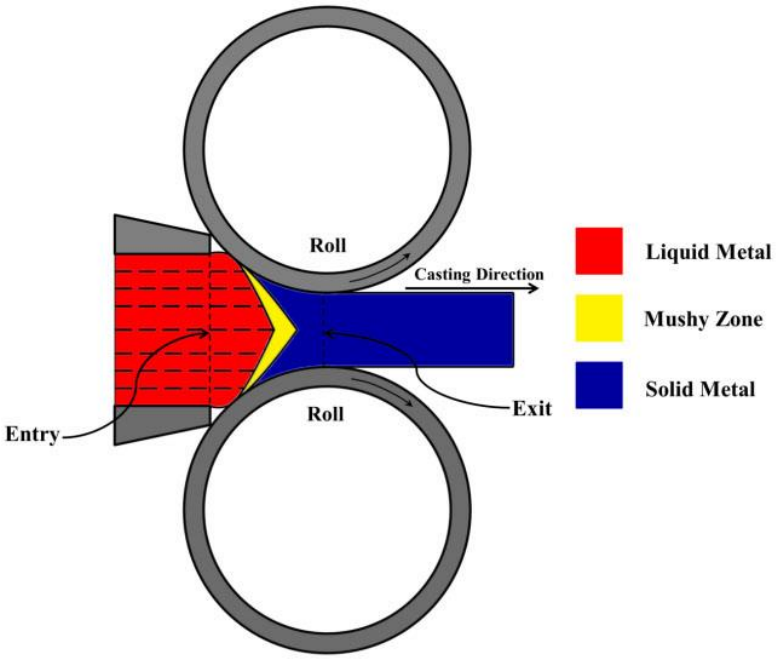

Figure 2.10 Representation of twin roll casting process [93]

Twin roll casting enables production of 5-6 mm thick magnesium alloy strip directly molten material. This provides huge time and cost saving. Moreover, improved microstructural properties can be achieved by twin roll casting.

2.3.3. Extrusion Machining

Extrusion-machining is a severe plastic deformation process to impose large-strain deformation induced by machining in the machined workpiece and chips [94]. This method could improve the disadvantages of magnesium alloys by one single processing step. It has emerged as an effective technique to produce ultrafine-grained microstructure for enhanced ductility and strength [95]. The schematic view of this deformation process as follows:

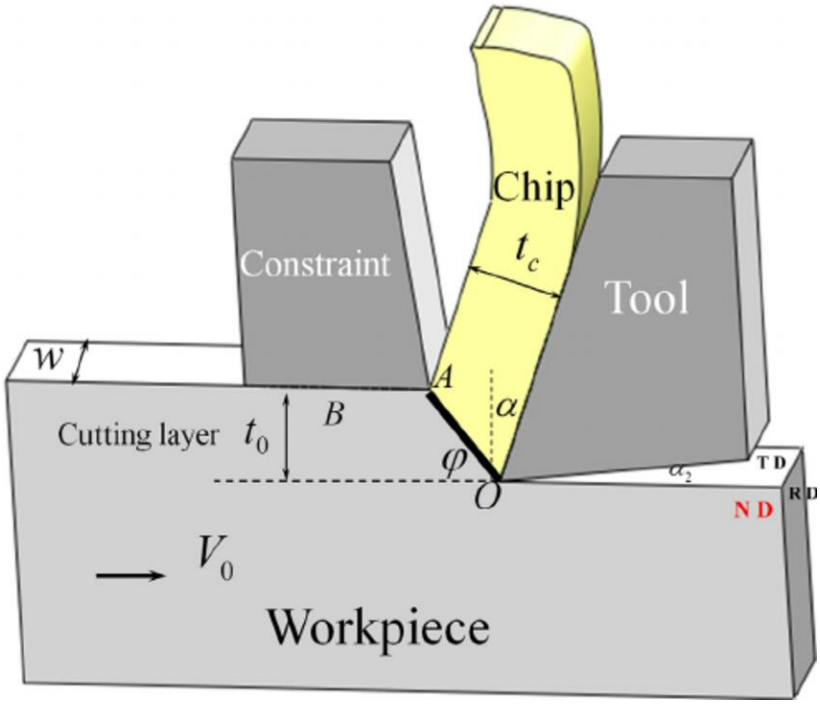

Figure 2.11 Schematic view of extrusion-machining [95]

where t_0 is cutting layer depth,

t_c is controlled chip thickness,

λ is chip thickness ratio ($\lambda = t_c/t_0$)

w is cutting width,

V_0 is cutting speed,

α is rake angle,

α_2 is clearance angle and

φ is shear angle.

The technique of EM has been demonstrated in Figure 2.11. While the sharp wedge-shaped tool with a rake angle α is static, the workpiece with a cutting layer depth travels at cutting speed V_0 toward the tool. Due to the process of shear in deformation

zone OA which is the region of intense strain rate, the workpiece materials in the cutting layer flow out in the form of a chip with a thickness t_c along the rake face of the tool [96]. The inclined angle φ of deformation zone is named as shear angle. To obtain different chip thickness ratios the position of constraint can be adjusted during EM.

Table 2.8 concludes up advantages and disadvantages of sheet deformation processes aforementioned above.

Table 2.8 Comparison of sheet deformation processes

Sheet Deformation Processes	**Advantages**	**Disadvantages**
Rolling	Commonly used Standard	Hard texture in final product Requirement of high temperature High scrap rate
Twin-Roll Casting	One step process Soft texture in final product Time saving process Lower cost	Challenging process Not applicable to low final thickness
Extrusion-machining	One step process Enhanced ductility and strength	Challenging process Needs high strain rates

2.4. Motivation and Aim of Study

Formability of magnesium alloys strictly depends on temperature, initial texture, strain rate and initial grain size. It is stated that AZ31 magnesium alloys need to be deformed at elevated temperature due to increased number of slip systems. At room temperatures only basal slip system is activated owing to low CRSS value and Schmid factor is zero in loading direction perpendicular to c-axis. Then twinning deformation mechanism

takes place which leads undesired defects such as twinning, shear band and even crack. Also, the fracture surface of magnesium alloy gives hint about the fracture types, it is fully ductile at elevated temperatures while it is quasi-brittle at room temperatures.

In addition to twinning, another limiting factor for low temperature formability is pronounced texture. Wrought magnesium alloys have a strong basal texture, alloying of magnesium with rare-earth elements both weakens the initial basal texture and decreases the CRSS of non-basal slip systems

The aim of this study is to understand and control the twinning-induced localization of magnesium sheets with basal, off-basal and mixed textures by rolling between room temperature and 165 ℃. While the fraction of flow localized regions increases from 0.1 to 0.6 with strain and temperature, the intensity of them are controlled by the starting textures. The interactive effects of starting texture and temperature are investigated to understand and control the twinning-induced shear banding during rolling. Another important goal of this study is to develop a texture and temperature dependent model for the twinning-induced softening phenomena. The model gives the maximum amount of deformation without shear banding, which results in uniform microstructures and defect-free final products.

CHAPTER 3

EXPERIMENTAL

3.1. Rolling Setup

Rolling of the AZ31 alloy was carried with an OAM CAVALLIN M120 shown in Figure 3.1 laboratory mill having 65 mm roll diameters. The rolling machine has a roll speed of 32 m/s and the desired true strain values were achieved by adjusting the rolls to the corresponding reduction by using relation of $\varepsilon = ln(t_0/t_f)$, where ε is the rolling strain per pass, t_0 is the initial thickness, and t_f is the final thickness.

Figure 3.1 OAM CAVALLIN M120

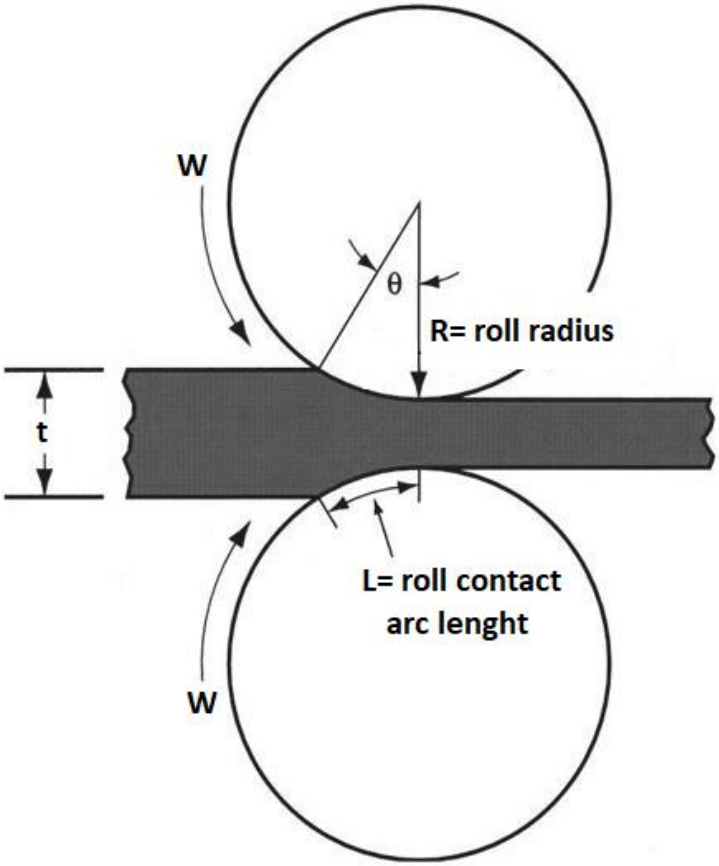

Figure 3.2 Schematic view of rolling process

Constant deformation rate was calculated as 3.5 /s by formula;

$$\dot{\varepsilon} = \frac{2\pi RW}{60}\frac{1}{L}\varepsilon \qquad (4)$$

where R is roll radius,

r is the fractional reduction thickness,

L is the roll contact arc length given by $L = \sqrt{Rrt}$,

t is the initial sheet thickness and

W is the roll rotation rate (rpm).

3.2. Temperature Data Logger Setup

The experiments were conducted at room temperature (RT) and the strips were pre-heated in closed to atmosphere furnace that is set to 100 ℃, 150 ℃ and 200 ℃. However, the actual deformation temperatures were lower due to heat losses to the air and the cold rolls of the mill. In order to measure the exact deformation temperatures 1 mm thermocouple wires were welded on both ends of the specimen. The wires were connected to a Natural Instruments ® data logger shown in

Figure 3.3, which recorded the temperatures during rolling with 6 s^{-1} Hz sampling frequency. Then, approximate deformation temperatures were taken as the average of entrance and exit temperatures for all experiments.

Figure 3.3 Natural Instruments data logger

3.3. Material and Methods

The materials investigated in the present work were commercially available Mg AZ31B alloy plates with 2 mm, 4 mm, 6 mm, and 7 mm thickness. They were received in hot-rolled and annealed condition (O temper) from Xi'an Yuechen Metal Products, Shaanxi, China. The 2 mm thick plate with dimensions of 150 mm (rolling direction; RD) x 20 mm (transverse direction; TD) x 2.2 mm (normal direction; ND) had a Vickers microhardness of 60.8±2.7 kg/mm². The plate exhibited strong basal texture as shown in the EBSD orientation map and accompanying pole figures (Figure 3.5a). The microstructure of the plate (rolling direction) consisted of equiaxed grains with an average grain size of 30±8 μm.

The 4 mm thick plate had also a strong basal texture. In order to have a different starting texture the 4 mm thick plate was rolled at 300 ℃ at a reduction of 30%. Then, it was annealed at 200 ℃ for eight hours to suppress heavily twinned microstructure. Since the EBSD results of 4 mm rolled and annealed specimen could not be seen clearly it was not possible to determine if the targeted initial texture is obtained. The reason behind this can be heavily twinned zones. That's why further investigation for 4 mm thick plate could not be done. Figure 3.4 shows the optical views of rolled and annealed 4 mm thick plate separately and EBSD result of annealed specimen.

The 6 mm thick plate showed a strong basal texture similar to the thinner plate. For the third investigate texture, this plate was sliced perpendicular to its normal direction by water-jet, resulting in strips with dimensions of 100 mm x 6 mm x 1.9 mm. In this orientation, the sliced strips had strong off-basal texture (Figure 3.5b). It had a hardness of 57.2±2.5 kg/mm², with uniform and equiaxed grain size of 33±8 μm (Figure 3.5b).

For the last investigated texture, the 7 mm thick plate was sliced perpendicular to its normal direction by water-jet. It had a strong basal texture similar to the thinner plates, but this time extension twins (86º misorientation) occupied about 50% of the microstructure (Figure 3.5c). Therefore, this texture became average of the two

previous extreme textures and labeled as “mixed” throughout the text. This type of texture can also be obtained by pre-rolling magnesium sheets to small reductions and it has been demonstrated to improve formability [97]. Plate with the mixed texture had dimensions of 100 mm (rolling direction; RD) x 7 mm (transverse direction; TD) x 1.9 mm (normal direction; ND) and had a Vickers microhardness of 60.8±2.7 kg/mm². Compared to the thinner plates, the grain size was larger and non-uniform (Figure 3.5c).

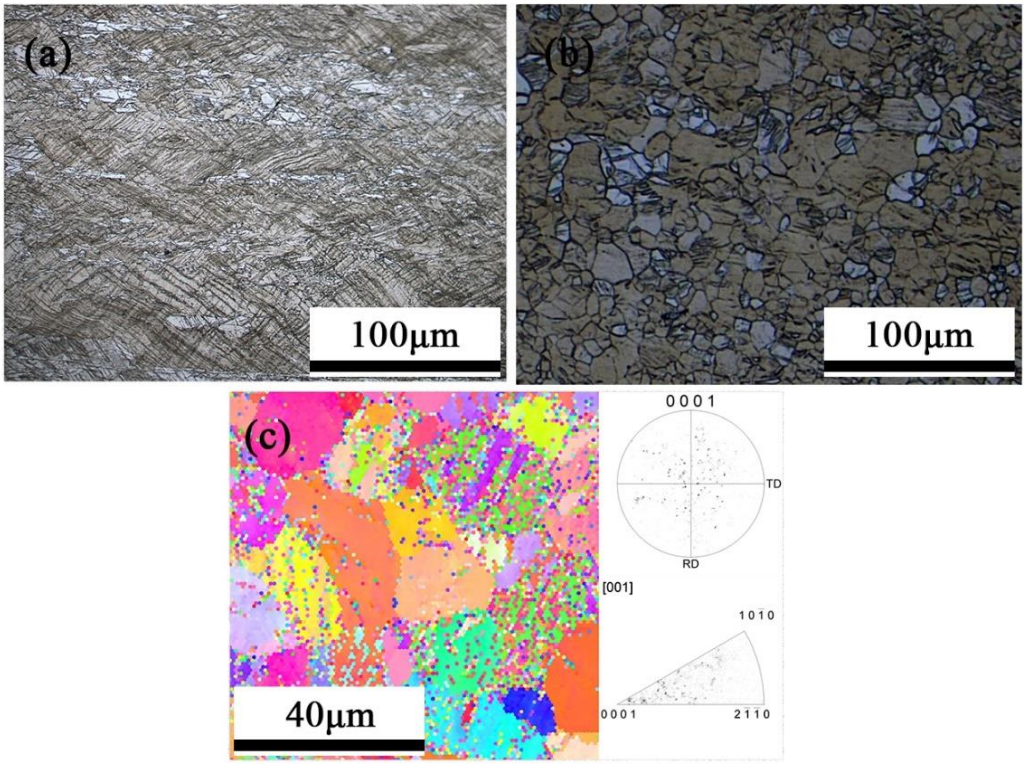

Figure 3.4 Optical views of a) rolled and b) rolled ad annealed and c) EBSD result of rolled and annealed 4 mm thick plate

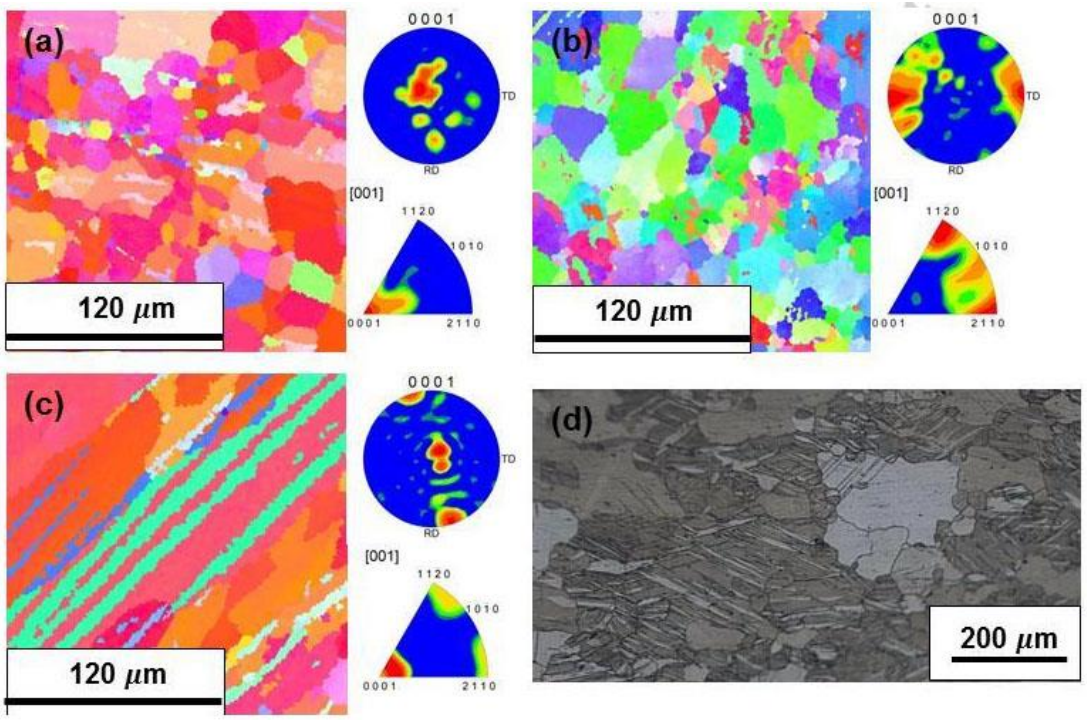

Figure 3.5 EBSD orientation maps, the associated pole figures and inverse pole figures from RD-TD planes of a) basal, b) off-basal and c) mixed textured strips before rolling. Optical micrograph (d) shows the nonuniform microstructure of the mixed texture

The microstructures of as-received and rolled samples were characterized by optical microscopy and electron backscatter diffraction (EBSD). For optical microscopy, the samples were etched with a solution of 9.5 g picric acid, 100 ml ethanol, 7.5 ml water and 3.5 ml acetic acid for about 30 s. Etching revealed the grain boundaries, twin boundaries and the strain-localized regions. Average grain size was also measured from the optical microstructures with ASTM E112 the linear intercept method. The optical as-received images of the 2 mm, 6 mm and 7 mm samples are shown in Figure 3.6. Figure 3.6a contains larger grains than 30 μm, there can be two different reasons behind this, either large grains were not affected during etching process or this microstructure contains some non-homogenous grains. In order to improve this microstructure view, etching time can be extended.

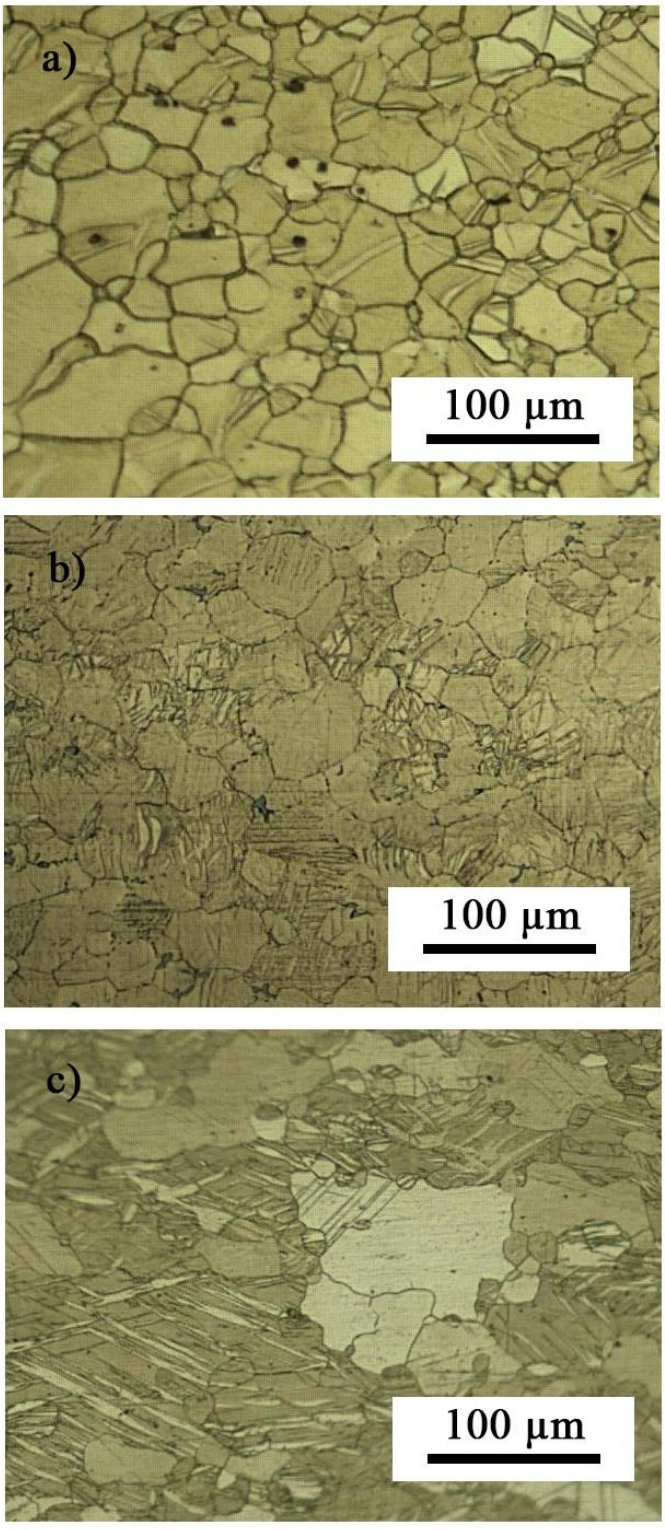

Figure 3.6 The optical as-received images of the a) 2 mm, b) 6 mm and c) 7 mm samples

Strain-localized fraction was measured by Adobe Photoshop ® software by using magic wand tool with a moderate tolerance adjusted with respect to the surrounding microstructure. The strain-localized area fraction was accepted as the ratio of marked pixels over whole pixels of the microstructure picture. A representative localized strain area calculation that belongs to 2 mm thick sample rolled at 150 ℃ is demonstrated in Figure 3.7. Then, the strain-localized area fraction was calculated as 0.352.

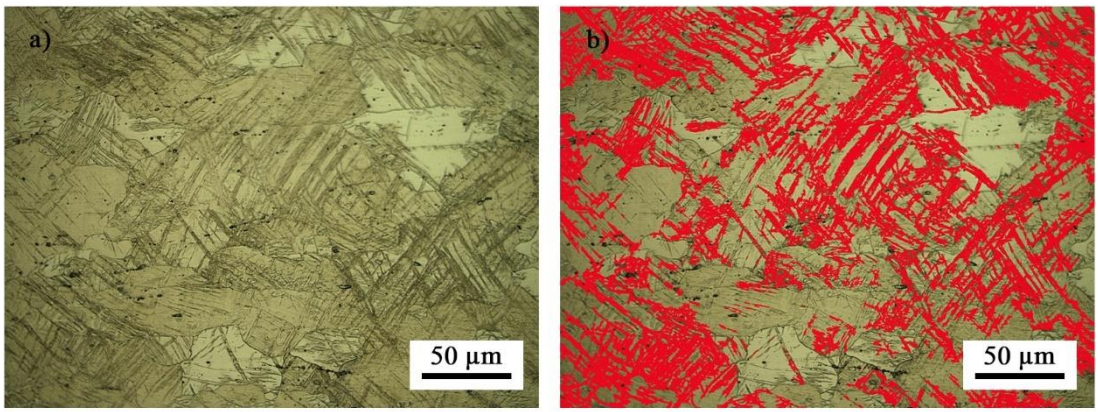

Figure 3.7 Demonstration of calculation of the strain-localized fraction by using Adobe Photoshop Software ®

For EBSD analysis, the samples were either electropolished with a 20% Nital solution at 35 V and −15 ℃ for about 10 s, or mechanically polished with a colloidal silica solution. A FEI Quanta 200 FX scanning electron microscope equipped with EDAX EBSD camera and OIM software was used for the EBSD analysis.

Three different samples were rolled at 0.05 strain increments until they failed by cracking at the edges. Samples deformed to the desired strain value in a single-pass, meaning the strains were not accumulative. A different sample was used for each tested strain value.

The experiments were conducted either at room temperature (RT) or by pre-heating the strips in furnace that is set to 100 ℃, 150 ℃ and 200 ℃. Since the actual

deformation temperatures were lower due to heat losses to the air and to the cold rolls of the mill, the actual deformation temperatures were measured by temperature data logger setup which is mentioned above. Figure 3.8 shows the temperature evolution during rolling of the sample pre-heated to 150 ℃.

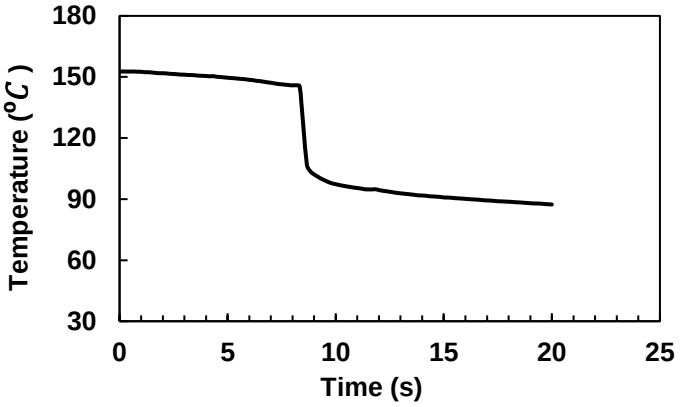

Figure 3.8 Temperature distribution during the rolling experiment with a pre-heating temperature of 150 ℃

The initial temperature decreases to 90 ℃ right after the rolling and the average of entrance and exit temperatures correspond to the deformation temperature. Similar trends were observed for the other pre-heating temperatures and the approximate deformation temperatures were taken as the average of entrance and exit temperatures for all experiments. Therefore, the samples were assumed to be rolled at RT, 80 ℃, 120 ℃ and 165 ℃.

CHAPTER 4

RESULTS AND DISCUSSION

4.1. Shear Banding in Rolling and Its Control

Figure 4.1 shows the positive effect of temperature on the maximum possible rolling strains per pass for each starting texture. Below the maximum strain, the sheets are continuous and sustain the specified strain in single-pass. At the maximum strain, samples crack from the edges. Strips shatter into pieces and become discontinuous above the maximum strains. As expected, all the samples with different textures can withstand to larger strains per pass as the temperature increases. At a given temperature, however, there is almost a two times difference between the maximum strains of the off-basal and basal starting textures. This difference increases at the higher temperatures. Samples with the off-basal and mixed textures are more sensitive to the temperature and become significantly more formable after 120 ℃, whereas the formability of the basal texture increases moderately with increasing temperature. Figure 4.2 belongs to basal textured specimen. True strain of the material increasing with the rising temperature. The maximum true strain the material withstand without cracking is seen as 0.32.

The increased temperature sensitivity in the off-basal and mixed textures may be due to the activation of non-basal slip at lower temperatures [31]. Off-basal textured sample contains some small grains that have favorable orientations for basal slip (Figure 3.5a). This slip can accumulate at the grain boundaries and trigger the activation of the non-basal slip at the boundaries. Mixed textured sample, on the other hand, contains additional twin boundaries (Figure 3.5c) and the non-basal clip can be triggered near the twin boundaries.

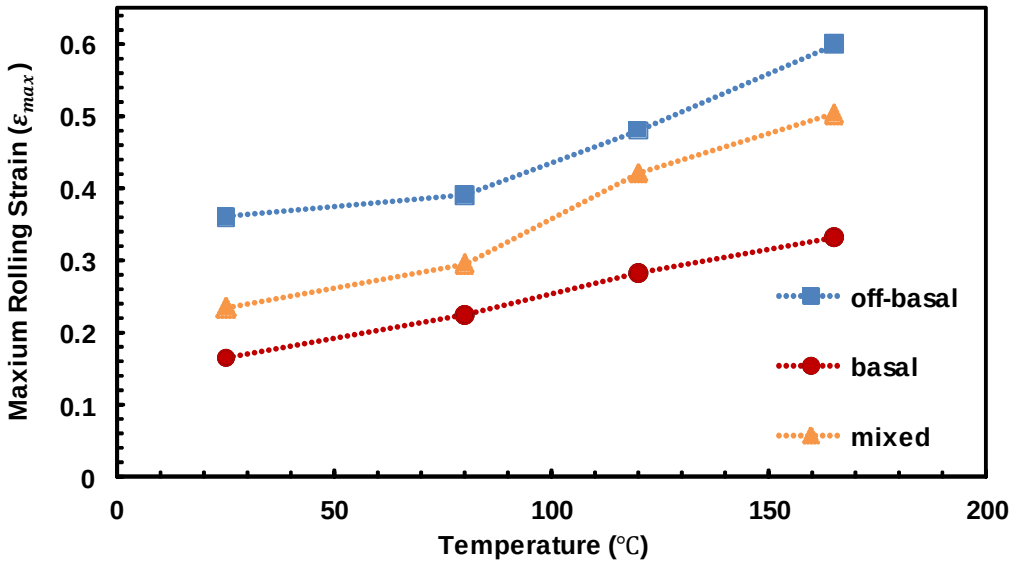

Figure 4.1 Maximum rolling strain per pass vs. temperature of basal, mixed and off-basal textured specimens

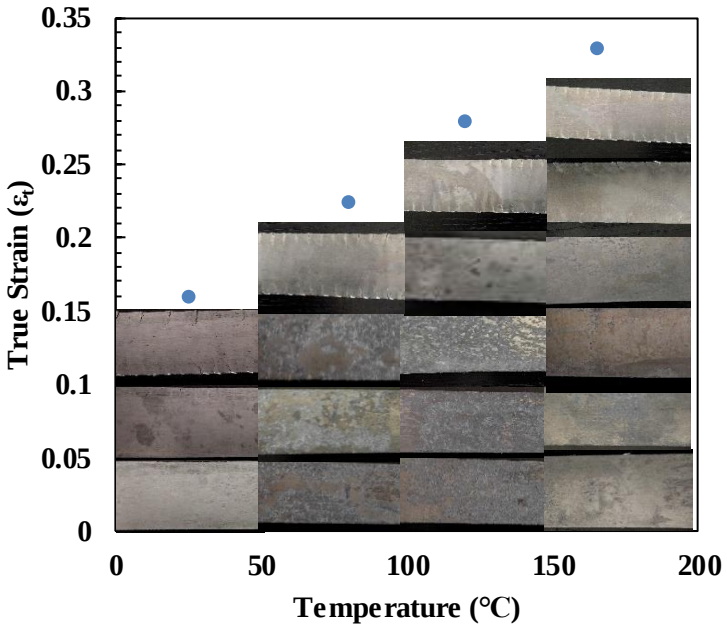

Figure 4.2 True strain per pass vs. temperature of basal texture specimen

Figure 4.3 compares the optical microstructures of sound and cracked strips that are rolled to ε = 0.12 and 0.37 at 120 ℃. Individual twins are distinct and visible in the microstructure of the sound strip (Figure 4.3a), whereas the cracked one has shear bands and a nonuniform microstructure (Figure 4.3b). While there may be twins in the shear bands, they already formed an interconnected network, resulting in the shear bands that are aligned 45° to the loading direction. Darker etching of the bands confirms the concentration of deformation within the bands. In addition, alignment of the bands is consistent with the maximum shear directions. The bands extend through the entire cross-section and result in the edge cracks as shown in the inset of Figure 4.3b. There are no visible cracks in the sound strip (inset of Figure 4.3a), and the deformation is relatively homogeneous despite the considerable twinning activity.

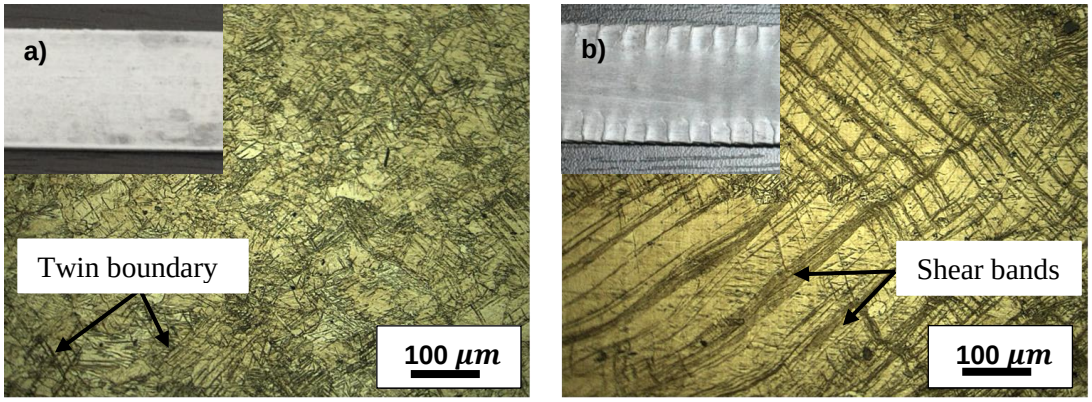

Figure 4.3 Optical microstructures of basal textured strips rolled at 120 ℃ a) ε = 0.12, sound strip (inset) b) ε = 0.37, cracked strip (inset). For the cracked strip, the inset shows a piece of the strip, as in this case edge cracking was severe and shattered the strip into small pieces

When the microstructures of basal and off-basal textures are compared at 80 ℃ and at a strain of 0.22, they appear to be similar. They both contain a high fraction of twins and concentration of deformation within the twinned areas (Figure 4.4). However, the basal textured sample shows a higher concentration of strain to the twins (Figure 4.4a), resulting in edge cracks at this temperature and strain. Off-basal sample is sound at $\varepsilon = 0.22$ and deforms uniformly until $\varepsilon = 0.39$ at this temperature. The twinned areas appear to accumulate a lower amount of strain, as the boundaries remain sharp

and the twins are narrow (Figure 4.4b). However, in the basal textured sample, the strain-localized areas are wider and they have darker contrast, indicating the formation of shear bands (Figure 4.4b). These results underline the importance of starting texture in suppressing twinning-induced shear bands. Starting texture offers a great improvement in formability, given that it is possible to produce Mg feedstock with the desired texture. The texture has great influence on the active deformation mechanisms, including the twinning [98]. Therefore, the level of twinning should be compared for each texture at various temperatures.

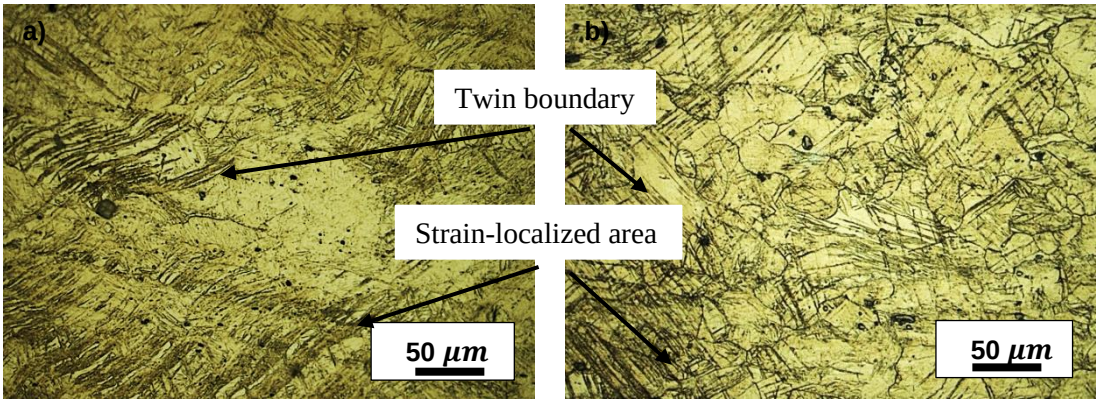

Figure 4.4 Optical microstructures of a) basal textured and b) off-basal textured strips rolled at 80 ℃ to 0.22 strain

4.2. Strain, Temperature and Texture Dependence of the Twinning Activity

One indication of the twinning activity is the fraction of the strain- localized regions (f). In Figure 4.5, the experiment done at two different strains of 0.09 and 0.19 demonstrates the increase in the volume fraction of the darkly etched regions with strain. While these regions do not necessarily correlate with the twins, they indicate slip within these areas. The microstructure may consist of more twins, which may not response to the etching. Tensile twins that can sometimes happen under compression may not react to etching [98]. In addition, twins may consume entire grains and leave no trail behind them [98,99]. Therefore, darkly etched regions provide indirect evidence to twinning-induced softening activity and may not represent the actual

fraction of the twinned areas. Still, it is possible to establish a relation between f and the strain, as first suggested by Barnett for Mg [32]: $f = C\varepsilon^2$, where C is the twinning rate constant depending on factors such as grain size and temperature. As the global strain increases, a higher fraction of deformation concentrates into the regions that are presumably twins.

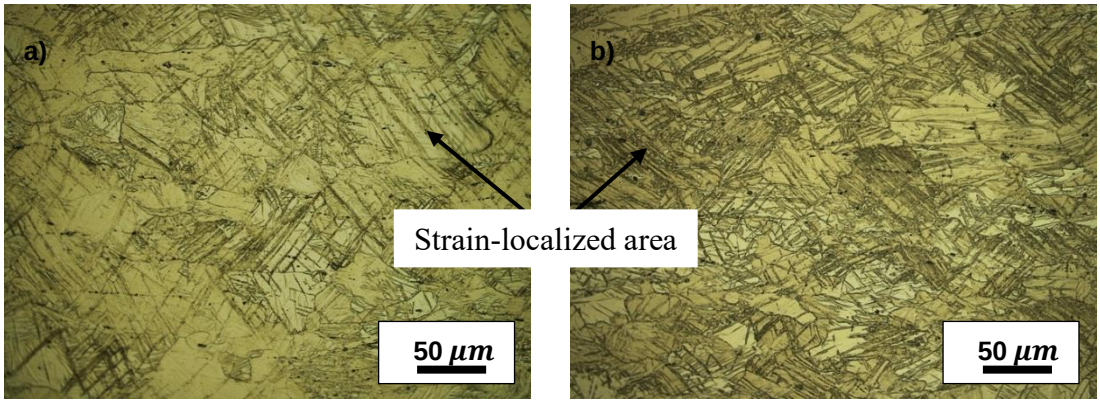

Figure 4.5 Optical microstructures of basal textured strips rolled at 150 ℃ to a strain of a) 0.09 b) 0.19

Figure 4.6 shows the effect of increasing temperature on f at constant strain for the basal texture. The microstructure at the higher temperature contains higher fraction of darkly-etched regions (Figure 4.6b). This result suggests higher twinning activity at the higher temperature and seems to contradict the common assumption of twinning suppression with increasing temperature.

However, the real effect of temperature is on the twinning rate constant, C. To investigate this, f is plotted over a wide range of strains at different temperatures (Figure 4.7a). Unlike the $f = C\varepsilon^2$ relation, results from Figure 4.7a yield a linear relationship between the f and ε: $f = C\varepsilon$. More importantly, C strongly depends on the temperature, almost diminishing at higher T. While there appears to be more twins at the higher temperatures, their fraction slightly increases with increasing strain. At lower temperatures, on the other hand, the fraction of twinned and strain-localized

regions is strongly sensitive to the strain since there are no other parameters to control deformation.

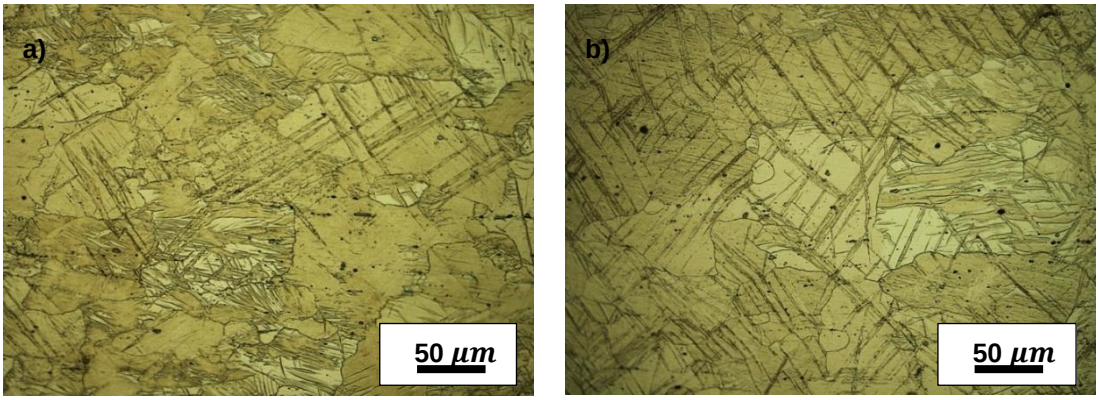

Figure 4.6 Optical microstructures of basal textured strips rolled at strain of 0.09 a) at room temperature, b) at 120 ℃

Fraction of strain-localized regions in basal, mixed and off-basal textures at various strain and temperatures are plotted in Figure 4.7, respectively. Similar to the basal texture, f increases with strain and temperature. The twinning rate constants seem to be independent of textures, and absolute values of the fractions are similar. There is only a slight deviation in the off-basal texture at 165 ℃, however there is a good agreement in the textures for the other temperatures. This allows the following empirical relationship between temperature and $C = 2.8exp(-0.013T)$, where T is in ℃. This equation is valid for each starting texture and it is remarkably similar to the equation fitted ($C = 3exp(-0.015T)$) to the experiments of Barnett on the effects of increasing strain on the twinned fraction [32,96]. By using this relationship and $f = C\varepsilon$, it is now possible to find the fraction twins, and therefore strain-localized regions, at a given temperature and strain. The starting texture has no effect on the f, yet it influences the extent of shear banding and cracking in the strips. Note that this equation is not valid when the strain equals to zero. While strain equals to zero strain localized fraction value should be zero.

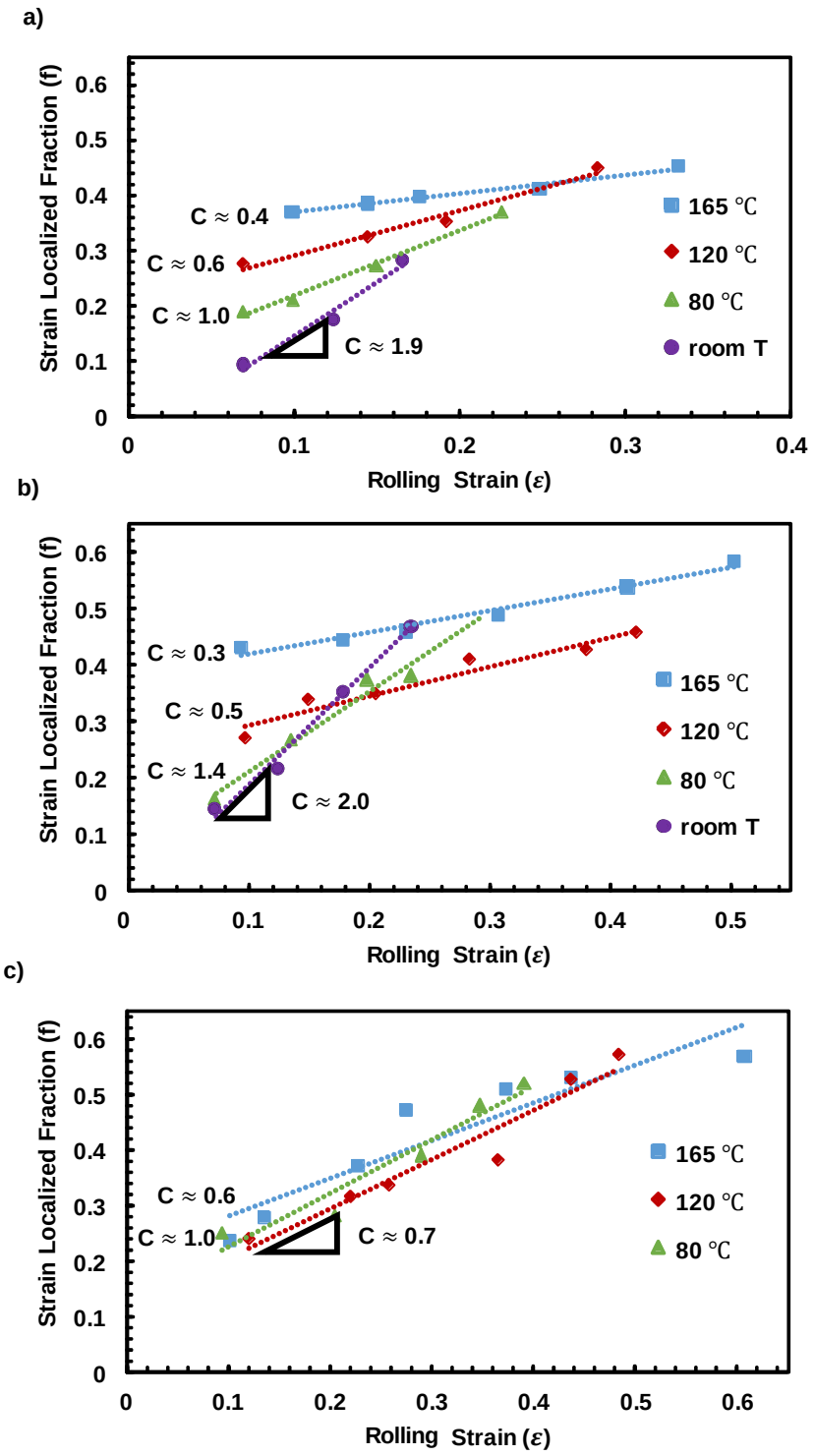

Figure 4.7 Area fraction of the strain-localized regions at various strain and temperatures for a) basal, b) mixed and c) off-basal textured samples

4.3. Twinning-induced Softening and Its Relation to Shear Banding

Independent of their fraction, twins induce softening in the matrix of all starting textures. In this case, the samples can be considered as a composite consisting of "soft" (twins) and "hard" (matrix) region. The relative "softness" of the twinned regions, on the other hand, is different for each starting texture. One way of finding the extent of softening is to compare the ratio of Schmid factors of basal slip inside the twins and the matrix at a given loading condition, $S_r = S_t/S_m$ [32,96]. Here S_t and S_m are the Schmid factors for basal slip inside the twin (most favorable variant is considered) and the matrix, respectively. A higher softening factor, S_r, indicates the intensity of strain localization within the twins [96].

Figure 4.8 shows calculations of S_t and S_m from EBSD maps for basal (Figure 4.8a) and off-basal (Figure 4.8) textures. The EBSD maps belong to the cross-section of the samples and they were taken at low strain (0.09) and temperature (25 ℃) to clearly distinguish twins. For each texture, three separate twin and matrix pairs were analyzed and the reported values are the averages. Incidentally, all the selected twins were {10-12} tensile twins for both textures. This type of twinning is common for the off-basal textured samples compressed perpendicular to their c-axis [100]. Twinning is usually rapid in this case and they may consume the entire sample even at lower strains, reorienting texture to the basal [100]. EBSD map from this sample (Figure 4.8b), does not show any rapid twinning and complete reorientation of the initial texture. The starting texture was not as sharp (Figure 3.5b) compared to the other off-basal textures in the literature [101]. This may allow some slip in addition to the tensile twins when accommodating the deformation.

Although rare, tensile twinning can happen in the basal textured samples compressed parallel to their c-axis [102]. Compression and double twins are more common and responsible from deformation for the basal texture, but tensile twins can be observed within the compressive twins and consume them [36,103]. Moreover, the starting basal texture was not relatively sharp (Figure 3.5a), again allowing slip and tensile

twinning in addition to the compression twins. Therefore, softening factors can be calculated from the tensile twins for both textures.

For the basal texture (Figure 4.8a), $S_m = 0.09$ and $S_t = 0.38$ yield a ratio of $S_r \approx 3.83$, indicating severe softening such that:

$$S_r = \frac{S_t}{S_m} = \frac{cos68cos23}{cos82cos47} = 3.83. \quad (5)$$

For the off-basal, there is slight softening, $S_r \approx 1.53$, according to the calculations in three different regions on the EBSD map. For the mixed texture, $S_r \approx 2.62$ is assumed without any calculations from EBSD maps, as this texture was the average of the basal and off-basal textures.

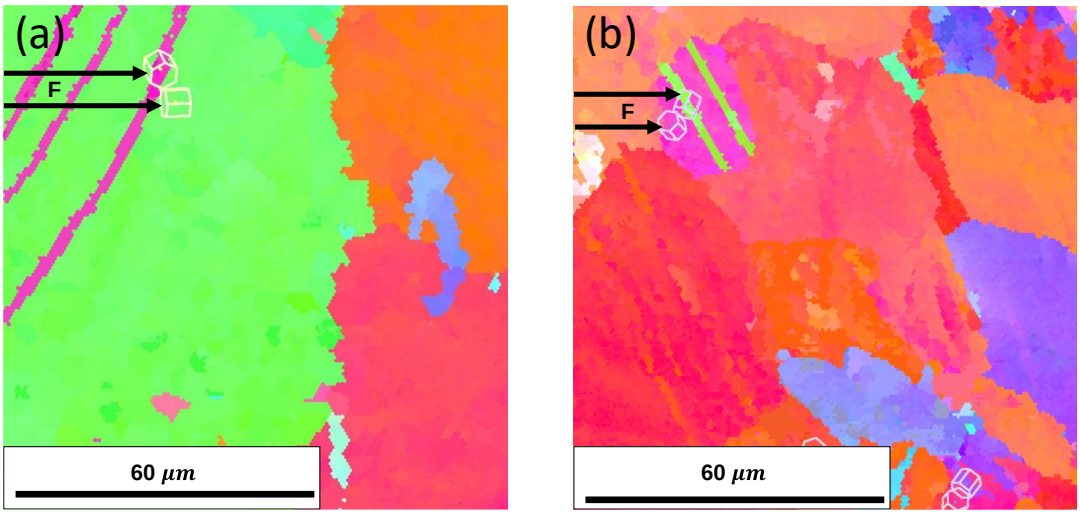

Figure 4.8 EBSD orientation maps of a) basal and b) off-basal textured specimens after rolling. In this case, EBSD maps are from the cross-section of the specimens (TD-ND plane) and the loading direction is shown with respect to the image plane

After finding the relative softness (S_r) and fraction (f) of each region, the continuum can now be treated as a composite, where each region has its own flow stress and strain. By using the iso-work (Iso-W) model, developed by Tóth et al. [104], the flow stress and strain in each region can be partitioned [96,104]. The model assumes that the plastic power is uniform in the continuum: $\dot{\varepsilon}\sigma = \dot{\varepsilon}_1\sigma_1 = \dot{\varepsilon}_2\sigma_2$, where subscripts 1 and 2 correspond to the matrix and twin fractions, respectively. In this case, the strain

rate in the twinned areas is higher due to the localizations. The partitioning factors r_i are defined by:

$$\dot{\varepsilon}_1 = r_1\dot{\varepsilon}, \quad \varepsilon_1 = r_1\varepsilon, \quad \dot{\varepsilon}_2 = r_2\dot{\varepsilon}, \quad \varepsilon_2 = r_2\varepsilon \tag{6}$$

$$(1-f)r_1 + fr_2 = 1 \tag{7}$$

where $f = C\varepsilon$. ε and $\dot{\varepsilon}$ for the twinned areas will be higher than for the matrix by the softening factor, S_r:

$$\frac{\varepsilon_2}{\varepsilon_1} = \frac{\dot{\varepsilon}_2}{\dot{\varepsilon}_1} = \frac{r_2}{r_1} = S_r \tag{8}$$

Using $\dot{\varepsilon}\sigma = \dot{\varepsilon}_1\sigma_1$, $\sigma_1 = K\varepsilon_1^n$ (K is the strength coefficient, n is the strain hardening exponent), and Eq. (6), flow stress of the composite is given by:

$$\sigma = Kr_1^{n+1}\varepsilon^n \tag{9}$$

where r_1 is found from Eqs. (7) and (8) as

$$r_1 = \frac{1}{(1-f)+fS_r}. \tag{10}$$

As fraction of the soft regions increases with strain, flow stress of the composite will become unstable after a critical strain. The onset of the instability can be determined by the Considère's criterion for compression:

$$\frac{1}{\sigma}\left(\frac{\partial\sigma}{\partial\varepsilon}\right) = -1. \tag{11}$$

Then, the maximum uniform strain before instability can be found by the following steps. The derivative of Eq. (9) is;

$$\frac{\partial\sigma}{\partial\varepsilon} = K\left(\frac{1}{1+\varepsilon A}\right)^{n+2}\varepsilon^{n-1}(n-\varepsilon A), \tag{12}$$

where A is defined as $C(S_r - 1)$. After finding the derivative, left side of the Equation 11 becomes:

$$\frac{1}{\sigma}\left(\frac{\partial\sigma}{\partial\varepsilon}\right) = \frac{(n-\varepsilon A)}{\varepsilon+\varepsilon^2}, \tag{13}$$

resulting in a uniform strain equation as a function of n, and A:

$$\varepsilon_u = -\frac{\sqrt{A^2+4An+2A+1}+A+1}{2A}. \tag{14}$$

Equation 14 gives the maximum uniform strain before instability under compression. However, start of instability does not necessarily trigger severe shear banding. In order to predict the onset of shear banding, the Considère's criterion is often modified by a strain localization parameter, α [105]. Several works in the literature suggested $\alpha \approx 5$ for initiation of severe shear banding, which leads to cracking [105,106]. Then, the maximum rolling strain becomes:

$$\varepsilon_{max} = -\alpha\varepsilon_u. \quad (15)$$

Strain hardening exponent in Equation 9, n, is assumed to be constant below 200 ℃ and taken as 0.15. The last modeling parameter, A, depends on the deformation temperature and starting texture. Experimental results show that the deformation temperature and strain control the fraction of the strain-localized regions through $f = C\varepsilon$ and $C = 2.8exp(-0.013T)$, whereas the starting texture controls the intensity of the localization with $S_r \approx 1.5$ for the off-basal, $S_r \approx 2.6$ for the mixed, and $S_r \approx 3.8$ for the basal textures.

Figure 4.9 shows the maximum rolling strains as a function of temperature and compares the model with experimental results for each texture. The dotted lines belong to experimental results while the continuous lines are fitted to model results. The model predicts slightly lower maximum strains compared to the experiments. While the match between the model and experiments is best for the basal texture, the difference between them is at most 10% for the other textures. The model applies to any deformation geometry and the starting texture, through the S_r, which can be calculated from EBSD maps obtained after small deformation at low temperatures. Alternatively, the active twinning system can be found from crystal-plasticity simulations, alleviating the need for extensive characterization experiments. In the most severe texture and deformation geometry combinations leading to shear banding, S_r can raise up to 5 [96]. On the other extreme, $S_r = 1$ when there is no softening. Finally, the model is valid below 200 ℃ where twinning is active. The model also considers basal slip as the only slip mode, however other non-basal systems can be active below 200 ℃ especially for the weaker starting textures.

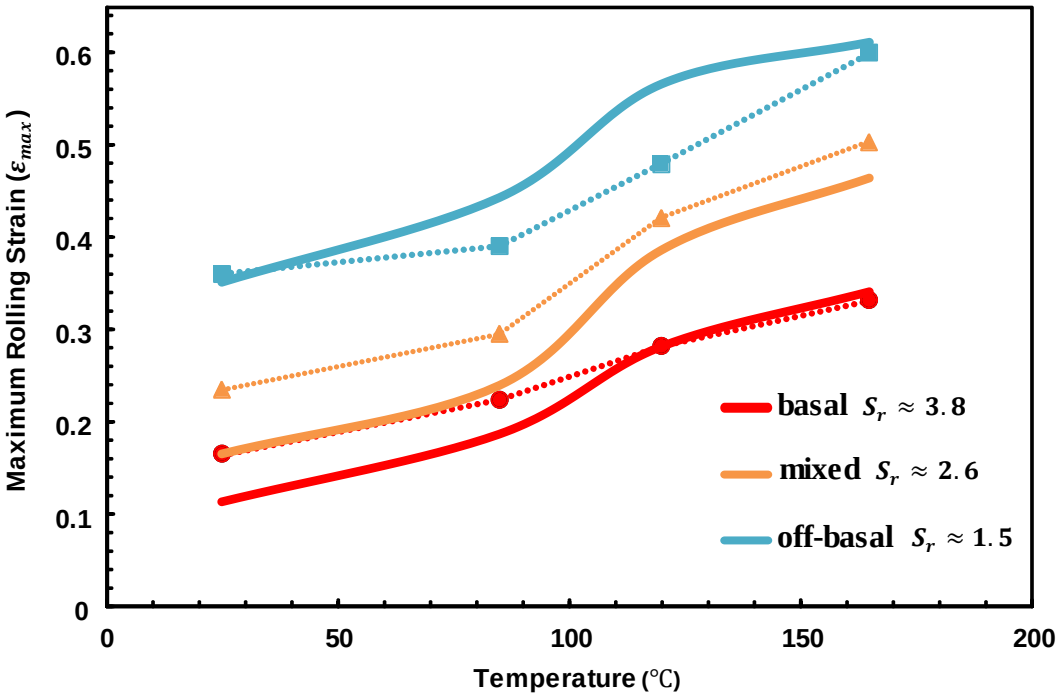

Figure 4.9 Experiment and modeling comparison of the temperature and texture dependence of the maximum rolling strain

CHAPTER 5

SUMMARY & FUTURE WORKS

Shear banding and failure during the rolling of magnesium sheets are investigated at different deformation temperatures (25-165 ℃) and starting textures. Twinning-induced strain localizations are linked to the shear banding and the maximum rolling strains. The interactive effects of twinning and strain localizations lead to the following key findings:

1) At a given temperature, samples with off-basal texture deform to almost 200% higher strains without shear banding compared to the basal textured samples. Mixed texture samples, on the other hand, result in ~ 50% higher rolling strains. The mixed texture is especially convenient in suppressing the shear banding as it can be obtained by pre-rolling. Increasing deformation temperature improves the formability of all the starting textures, where there is two times increase in the maximum strains from room temperature to 165 ℃.

2) For all starting textures, {10−12} tensile twins induce softening by reorienting the texture for favorable basal slip. Strain localizes into the twinned regions within an almost undeformed matrix. The extent of the localization is found by comparing the Schmid factors of basal slip within the twins and the matrix. The ratio of Schmid factors yields a softening ratio, S_r, and the twinned regions accumulate higher strains as S_r increases. When the individual twinning behavior is analyzed at all textures, the basal textured sample yields to highest $S_r \approx 3.8$. The sample with off-basal texture shows minimal softening with $S_r \approx 1.5$. In turn, basal textured samples develop intense strain localizations at earlier strains, and fail by shear banding and edge cracking.

3) The fraction of strain-localized areas increases with temperature and strain. At a given temperature and strain, however, the fraction of strain-localized regions is

independent of the starting texture. The real effect of the starting texture reveals itself on the intensity of strain localizations, which is controlled by the S_r.

4) Maximum strain before shear banding is both determined by experiments and modeling. The model treats the sample as a composite that contains soft twinned regions and hard matrix regions. After incorporating the fraction of twinning-induced localizations and their intensity into the model, it successfully captures the initiation of shear banding and results in similar maximum strains compared to the experiments.

REFERENCES

[1] H. Friedrich, S. Schumann, Research for a “new age of magnesium” in the automotive industry, J. Mater. Process. Technol. 117 (2001) 276–281. doi:10.1016/S0924-0136(01)00780-4.

[2] D. Eliezer, E. Aghion, F.H. (Sam) Froes, Magnesium Science, Technology and Applications, in: Adv. Perform. Mater., 1998: pp. 201–212. doi:10.1023/A:1008682415141.

[3] M.K. Kulekci, Magnesium and its alloys applications in automotive industry, Int. J. Adv. Manuf. Technol. 39 (2008) 851–865. doi:10.1007/s00170-007-1279-2.

[4] H.K. Abdel-Aal, H.K. Abdel-Aal, Commercial Methods for Magnesium Production, in: Magnesium, 2018. doi:10.1201/9781351170642-6.

[5] C. Blawert, N. Hort, K.U. Kainer, Automotive Applications of Magnesium and Its Alloys, Trans. Indian Inst. Met. 57 (2004) 397–408. doi:10.4028/www.scientific.net/MSF.419-422.67.

[6] F. Zarandi, S. Yue, Magnesium Sheet ; Challenges and Opportunities, Magnes. Alloy. - Des. Process. Prop. (2011) 297–320.

[7] E. Aghion, B. Bronfin, D. Eliezer, The role of the magnesium industry in protecting the environment, J. Mater. Process. Technol. 117 (2001) 381–385.

[8] J.J. Michalek, P.Y. Papalambros, S.J. Skerlos, A Study of Fuel Efficiency and Emission Policy Impact on Optimal Vehicle Design Decisions, J. Mech. Des. 126 (2004) 1062. doi:10.1115/1.1804195.

[9] M. Hakamada, T. Furuta, Y. Chino, Y. Chen, H. Kusuda, M. Mabuchi, Life cycle inventory study on magnesium alloy substitution in vehicles, Energy. 32 (2007) 1352–1360. doi:10.1016/J.ENERGY.2006.10.020.

[10] Automotive Uses of Magnesium Alloys: Part One :: Total Materia Article, (n.d.). https://www.totalmateria.com/page.aspx?ID=CheckArticle&site=ktn&NM=246 (accessed January 1, 2019).

[11] BMW Pushes Lightweight Technology with Magnesium, (n.d.).

http://www.worldcarfans.com/2030721.001/bmw-pushes-lightweight-technology-with-magnesium (accessed January 10, 2019).

[12] 10 Best Engines of 2006, (n.d.). https://www.wardsauto.com/news-analysis/10-best-engines-2006 (accessed January 10, 2019).

[13] Young's Modulus - Density, (n.d.). http://www-materials.eng.cam.ac.uk/mpsite/interactive_charts/stiffness-density/basic.html (accessed January 12, 2019).

[14] A. Dziubińska, A. Gontarz, M. Dziubiński, M. Barszcz, THE FORMING OF MAGNESIUM ALLOY FORGINGS FOR AIRCRAFT AND AUTOMOTIVE APPLICATIONS, Adv. Sci. Technol. Res. J. (2016). doi:10.12913/22998624/64003.

[15] M.R. Barnett, K.U. Kainer, A. Arslan Kaya, M.R. Barnett, Forming of magnesium and its alloys, in: Fundam. Magnes. Alloy Metall., Elsevier, 2013: pp. 197–231. doi:10.1533/9780857097293.197.

[16] M.M. Avedesian, H. Baker, ASM International. Handbook Committee., Magnesium and magnesium alloys, ASM International, 1999.

[17] J.F. Grandfield, Direct chill casting of magnesium extrusion billet and rolling slab, Woodhead Publishing Limited, 2012. doi:10.1016/B978-1-84569-968-0.50006-5.

[18] E. Aghion, G. Golub, Production Technologies of Magnesium, in: Magnes. Technol., Springer-Verlag, Berlin/Heidelberg, 2006: pp. 29–62. doi:10.1007/3-540-30812-1_2.

[19] D. Liang, C.B. Cowley, The twin-roll strip casting of magnesium, Jom. 56 (2004) 26–28. doi:10.1007/s11837-004-0122-6.

[20] R. V. Allen, D.R. East, T.J. Johnson, W.E. Borbidge, D. Liang, Magnesium Alloy Sheet Produced by Twin Roll Casting, in: Magnes. Technol. 2001, John Wiley & Sons, Inc., Hoboken, NJ, USA, 2013: pp. 74–79. doi:10.1002/9781118805497.ch15.

[21] E. Essadiqi, I.H. Jung, M.A. Wells, Twin roll casting of magnesium, Woodhead Publishing Limited, 2012. doi:10.1016/B978-1-84569-968-0.50007-7.

[22] M. Efe, W. Moscoso, K.P. Trumble, W. Dale Compton, S. Chandrasekar, Mechanics of large strain extrusion machining and application to deformation

processing of magnesium alloys, Acta Mater. (2012). doi:10.1016/j.actamat.2012.01.018.

[23] H. Watari, R. Paisarn, T. Haga, K. Noda, K. Davey, N. Koga, Development of manufacturing process of wrou- ght magnesium alloy sheets by twin roll casting, Manuf. Eng. (2007).

[24] Z. Yu, Y. Yan, J. Yao, C. Wang, M. Zha, X. Xu, Y. Liu, H. Wang, Q. Jiang, Effect of tensile direction on mechanical properties and microstructural evolutions of rolled Mg-Al-Zn-Sn magnesium alloy sheets at room and elevated temperatures, J. Alloys Compd. 744 (2018) 211–219. doi:10.1016/J.JALLCOM.2018.01.344.

[25] Z. Wang, R. Gu, S. Chen, W. Wang, X. Wei, Effect of upper-die temperature on the formability of AZ31B magnesium alloy sheet in stamping, J. Mater. Process. Technol. 257 (2018) 180–190. doi:10.1016/J.JMATPROTEC.2018.03.004.

[26] P.G. Partridge, The crystallography and deformation modes of hexagonal close-packed metals, Metall. Rev. (2014). doi:10.1179/mtlr.1967.12.1.169.

[27] B. c. Wonsiewicz, W.A. Backofen, PLASTICITY OF MAGNESIUM CRYSTALS, Trans. Metall. Soc. Aime. (1967).

[28] J.W. Christian, S. Mahajan, Deformation twinning, Prog. Mater. Sci. (1995). doi:10.1016/0079-6425(94)00007-7.

[29] T. Obara, H. Yoshinga, S. Morozumi, {1122} ⟨1123⟩ Slip system in magnesium, Acta Metall. (1973). doi:10.1016/0001-6160(73)90141-7.

[30] S.R. Agnew, C.N. Tomé, D.W. Brown, T.M. Holden, S.C. Vogel, Study of slip mechanisms in a magnesium alloy by neutron diffraction and modeling, Scr. Mater. 48 (2003) 1003–1008. doi:10.1016/S1359-6462(02)00591-2.

[31] M.H. Yoo, S.R. Agnew, J.R. Morris, K.M. Ho, Non-basal slip systems in HCP metals and alloys: Source mechanisms, Mater. Sci. Eng. A. (2001). doi:10.1016/S0921-5093(01)01027-9.

[32] M.R. Barnett, Twinning and the ductility of magnesium alloys. Part II. “Contraction” twins, Mater. Sci. Eng. A. (2007). doi:10.1016/j.msea.2007.02.109.

[33] Y.B. Chun, C.H.J. Davies, Texture effects on development of shear bands in

rolled AZ31 alloy, Mater. Sci. Eng. A. (2012). doi:10.1016/j.msea.2012.06.083.

[34] H. Yoshinaga, R. Horiuchi, Deformation Mechanisms in Magnesium Single Crystals Compressed in the Direction Parallel to Hexagonal Axis, Trans. Japan Inst. Met. (2014). doi:10.2320/matertrans1960.4.1.

[35] W.H. Hartt, R.E. Reed-Hill, Internal deformation and fracture of second order 1011-1012 twins in magnesium, Trans Met. Soc AIME. (1968).

[36] M.R. Barnett, M.D. Nave, C.J. Bettles, Deformation microstructures and textures of some cold rolled Mg alloys, Mater. Sci. Eng. A. (2004). doi:10.1016/j.msea.2004.07.030.

[37] O. Muránsky, M.R. Barnett, D.G. Carr, S.C. Vogel, E.C. Oliver, Investigation of deformation twinning in a fine-grained and coarse-grained ZM20 Mg alloy: Combined in situ neutron diffraction and acoustic emission, Acta Mater. (2010). doi:10.1016/j.actamat.2009.10.057.

[38] K. Hazeli, J. Cuadra, P.A. Vanniamparambil, A. Kontsos, In situ identification of twin-related bands near yielding in a magnesium alloy, Scr. Mater. (2013). doi:10.1016/j.scriptamat.2012.09.009.

[39] E. Kapan, N. Shafaghi, S. Uçar, C.C. Aydıner, Texture-dependent character of strain heterogeneity in Magnesium AZ31 under reversed loading, Mater. Sci. Eng. A. (2017). doi:10.1016/j.msea.2016.12.085.

[40] T. Al-Samman, K.D. Molodov, D.A. Molodov, G. Gottstein, S. Suwas, Softening and dynamic recrystallization in magnesium single crystals during c-axis compression, Acta Mater. (2012). doi:10.1016/j.actamat.2011.10.013.

[41] J. Bohlen, M.R. Nürnberg, J.W. Senn, D. Letzig, S.R. Agnew, The texture and anisotropy of magnesium-zinc-rare earth alloy sheets, Acta Mater. (2007). doi:10.1016/j.actamat.2006.11.013.

[42] B. Beausir, S. Biswas, D.I. Kim, L.S. Tóth, S. Suwas, Analysis of microstructure and texture evolution in pure magnesium during symmetric and asymmetric rolling, Acta Mater. (2009). doi:10.1016/j.actamat.2009.07.008.

[43] J.A. del Valle, F. Carreño, O.A. Ruano, Influence of texture and grain size on work hardening and ductility in magnesium-based alloys processed by ECAP and rolling, Acta Mater. (2006). doi:10.1016/j.actamat.2006.05.018.

[44] C.Y. Lin, H.J. Tsai, C.G. Chao, T.F. Liu, Effects of equal channel angular extrusion on the microstructure and high-temperature mechanical properties of ZA85 magnesium alloy, J. Alloys Compd. (2012). doi:10.1016/j.jallcom.2012.03.107.

[45] K. Xia, J.T. Wang, X. Wu, G. Chen, M. Gurvan, Equal channel angular pressing of magnesium alloy AZ31, Mater. Sci. Eng. A. (2005). doi:10.1016/j.msea.2005.08.123.

[46] S.R. Agnew, J.A. Horton, T.M. Lillo, D.W. Brown, Enhanced ductility in strongly textured magnesium produced by equal channel angular processing, Scr. Mater. (2004). doi:10.1016/j.scriptamat.2003.10.006.

[47] C. Drouven, I. Basu, T. Al-Samman, S. Korte-Kerzel, Twinning effects in deformed and annealed magnesium-neodymium alloys, Mater. Sci. Eng. A. (2015). doi:10.1016/j.msea.2015.08.090.

[48] J. Koike, T. Kobayashi, T. Mukai, H. Watanabe, M. Suzuki, K. Maruyama, K. Higashi, The activity of non-basal slip systems and dynamic recovery at room temperature in fine-grained AZ31B magnesium alloys, Acta Mater. (2003). doi:10.1016/S1359-6454(03)00005-3.

[49] M.H. Yoo, Slip, twinning, and fracture in hexagonal close-packed metals, Metall. Trans. A. (1981). doi:10.1007/BF02648537.

[50] H.E. Friedrich, B.L. Mordike, Magnesium technology: Metallurgy, design data, applications, 2006. doi:10.1007/3-540-30812-1.

[51] W. Callister Jr., D. Rethwisch, Fundamentals of Materials Science and Engineering: An Integrated Approach, 2013.

[52] M. Pekguleryuz, K. Kainer, A.A. Kaya, Fundamentals of magnesium alloy metallurgy, 2013. doi:10.1533/9780857097293.

[53] E.P. (Ernest P. DeGarmo, J.T. Black, R.A. Kohser, Degarmo’s materials and processes in manufacturing, 2017.

[54] Materials and processes in manufacturing, J. Manuf. Syst. (2008). doi:10.1016/s0278-6125(98)80067-8.

[55] E. Karimi, A. Zarei-Hanzaki, M.H. Pishbin, H.R. Abedi, P. Changizian, Instantaneous strain rate sensitivity of wrought AZ31 magnesium alloy, Mater. Des. (2013). doi:10.1016/j.matdes.2013.01.068.

[56] Temper Designations of Magnesium Alloys, Cast and Wrought, (n.d.). https://www.totalmateria.com/page.aspx?ID=CheckArticle&site=ktn&NM=34 (accesed March 5, 2019).

[57] C.L. Mendis, K. Hono, Understanding precipitation processes in magnesium alloys, Woodhead Publishing Limited, 2013. doi:10.1533/9780857097293.125.

[58] M. Pekguleryuz, Alloying behavior of magnesium and alloy design, Woodhead Publishing Limited, 2013. doi:10.1533/9780857097293.152.

[59] R. Neelameggham, Primary production of magnesium, Woodhead Publishing Limited, 2013. doi:10.1533/9780857097293.1.

[60] G. Neite, K. Kubota, K. Higashi, F. Hehmann, Magnesium-Based Alloys, in: Mater. Sci. Technol., 2006. doi:10.1002/9783527603978.mst0082.

[61] F. R, S. A, D. S, Magnesium alloys containing rare earth metals: structure and properties, 2003.

[62] Magnesium Alloys Overview, (n.d.). https://www.intlmag.org/page/design_mag_all_ima/Magnesium-Alloys-Overview.htm (accesed October 1, 2019).

[63] Y. Ding, C. Wen, P. Hodgson, Y. Li, Effects of alloying elements on the corrosion behavior and biocompatibility of biodegradable magnesium alloys: A review, J. Mater. Chem. B. (2014). doi:10.1039/c3tb21746a.

[64] E. Dogan, S. Wang, M.W. Vaughan, I. Karaman, Dynamic precipitation in Mg-3Al-1Zn alloy during different plastic deformation modes, Acta Mater. 116 (2016) 1–13. doi:10.1016/j.actamat.2016.06.011.

[65] K. Yu, Z.Y. Cai, X.Y. Wang, T. Shi, W.X. Li, Constitutive analysis of AZ31 magnesium alloy plate, J. Cent. South Univ. Technol. (English Ed. (2010). doi:10.1007/s11771-010-0002-x.

[66] Azom, Magnesium AZ31B Alloy (UNS M11311), AZoNetwork UK. (2012) 1–2.

[67] B.L. Mordike, T. Ebert, Magnesium Properties - applications - potential, Mater. Sci. Eng. A. 302 (2001) 37–45. doi:10.1016/S0921-5093(00)01351-4.

[68] Q. Yang, B. Jiang, J. Li, H. Dong, W. Liu, S. Luo, F. Pan, Modified texture and room temperature formability of magnesium alloy sheet by Li addition, Int. J. Mater. Form. 9 (2016) 305–311. doi:10.1007/s12289-014-1211-x.

[69] C.S. (Charles S. Barrett, T.B. Massalski, Structure of metals : crystallographic methods, principles, and data, 1966. doi:10.1126/science.117.3042.421-a.

[70] U.F. Kocks, The relation between polycrystal deformation and single-crystal deformation, Metall. Mater. Trans. 1 (1970) 1121–1143. doi:10.1007/BF02900224.

[71] J.P. Hadorn, K. Hantzsche, S. Yi, J. Bohlen, D. Letzig, J.A. Wollmershauser, S.R. Agnew, Role of solute in the texture modification during hot deformation of Mg-rare earth alloys, Metall. Mater. Trans. A Phys. Metall. Mater. Sci. 43 (2012) 1347–1362. doi:10.1007/s11661-011-0923-5.

[72] X.Y. Lou, M. Li, R.K. Boger, S.R. Agnew, R.H. Wagoner, Hardening evolution of AZ31B Mg sheet, Int. J. Plast. 23 (2007) 44–86. doi:10.1016/j.ijplas.2006.03.005.

[73] Z. Keshavarz, M.R. Barnett, EBSD analysis of deformation modes in Mg-3Al-1Zn, Scr. Mater. 55 (2006) 915–918. doi:10.1016/j.scriptamat.2006.07.036.

[74] M.R. Barnett, Twinning and the ductility of magnesium alloys. Part I: “Tension” twins, Mater. Sci. Eng. A. 464 (2007) 1–7. doi:10.1016/j.msea.2006.12.037.

[75] A. Jain, S.R. Agnew, Modeling the temperature dependent effect of twinning on the behavior of magnesium alloy AZ31B sheet, Mater. Sci. Eng. A. 462 (2007) 29–36. doi:10.1016/j.msea.2006.03.160.

[76] S.G. Hong, S.H. Park, C.S. Lee, Role of {10-12} twinning characteristics in the deformation behavior of a polycrystalline magnesium alloy, Acta Mater. 58 (2010) 5873–5885. doi:10.1016/j.actamat.2010.07.002.

[77] H. El Kadiri, J. Kapil, A.L. Oppedal, L.G. Hector, S.R. Agnew, M. Cherkaoui, S.C. Vogel, The effect of twin-twin interactions on the nucleation and propagation of { 1 0 1¯2 } twinning in magnesium, Acta Mater. 61 (2013) 3549–3563.

[78] E. Asadi, M. Asle Zaeem, The anisotropy of hexagonal close-packed and liquid interface free energy using molecular dynamics simulations based on modified embedded-atom method, Acta Mater. (2016). doi:10.1016/j.actamat.2016.01.043.

[79] X.L. Nan, H.Y. Wang, L. Zhang, J.B. Li, Q.C. Jiang, Calculation of Schmid factors in magnesium: Analysis of deformation behaviors, Scr. Mater. 67

(2012) 443–446. doi:10.1016/j.scriptamat.2012.05.042.

[80] X. Liu, J.J. Jonas, L.X. Li, B.W. Zhu, Flow softening, twinning and dynamic recrystallization in AZ31 magnesium, Mater. Sci. Eng. A. 583 (2013) 242–253. doi:10.1016/j.msea.2013.06.074.

[81] M.R. Barnett, A Taylor model based description of the proof stress of magnesium AZ31 during hot working, Metall. Mater. Trans. A Phys. Metall. Mater. Sci. 34 A (2003) 1799–1806. doi:10.1007/s11661-003-0146-5.

[82] G.I. Taylor, Plastic strain in metals, Twenty-Eighth May Lect. to Inst. Met. (1938). doi:not found.

[83] S.R. Agnew, M.H. Yoo, C.N. Tomé, Application of texture simulation to understanding mechanical behavior of Mg and solid solution alloys containing Li or Y, Acta Mater. 49 (2001) 4277–4289. doi:10.1016/S1359-6454(01)00297-X.

[84] R.E. Reed-Hill, W.D. Robertson, Deformation of magnesium single crystals by non basal slip, AIME Trans. 496 (1957) 496–502.

[85] J. Geng, M.F. Chisholm, R.K. Mishra, K.S. Kumar, An electron microscopy study of dislocation structures in Mg single crystals compressed along [0 0 0 1] at room temperature, Philos. Mag. 95 (2015) 3910–3932. doi:10.1080/14786435.2015.1108531.

[86] R. Gehrmann, M.M. Frommert, G. Gottstein, Texture effects on plastic deformation of magnesium, Mater. Sci. Eng. A. (2005). doi:10.1016/j.msea.2005.01.002.

[87] W.J. Kim, J.B. Lee, W.Y. Kim, H.T. Jeong, H.G. Jeong, Microstructure and mechanical properties of Mg-Al-Zn alloy sheets severely deformed by asymmetrical rolling, Scr. Mater. (2007). doi:10.1016/j.scriptamat.2006.09.034.

[88] S.R. Agnew, Ö. Duygulu, Plastic anisotropy and the role of non-basal slip in magnesium alloy AZ31B, Int. J. Plast. 21 (2005) 1161–1193. doi:10.1016/j.ijplas.2004.05.018.

[89] Y. Chino, K. Kimura, M. Mabuchi, Deformation characteristics at room temperature under biaxial tensile stress in textured AZ31 Mg alloy sheets, Acta Mater. 57 (2009) 1476–1485. doi:10.1016/j.actamat.2008.11.033.

[90] H. Qiao, X.Q. Guo, S.G. Hong, P.D. Wu, Modeling of {10-12}-{10-12} secondary twinning in pre-compressed Mg alloy AZ31, J. Alloys Compd. (2017). doi:10.1016/j.jallcom.2017.07.133.

[91] H. Koh, T. Sakai, H. Utsunomiya, S. Minamiguchi, Deformation and Texture Evolution during High-Speed Rolling of AZ31 Magnesium Sheets, Mater. Trans. (2007). doi:10.2320/matertrans.l-mra2007875.

[92] Z. Zhang, M.P. Wang, N. Jiang, S. Zhu, Formation of shearing bands in the hot-rolling process of AZ31 alloy, J. Alloys Compd. (2012). doi:10.1016/j.jallcom.2011.09.021.

[93] A. Hadadzadeh, Mathematical Modeling of the Twin Roll Casting Process for Magnesium Alloy AZ31, University of Waterloo, 2013.

[94] R. Bertolini, S. Bruschi, A. Ghiotti, L. Pezzato, M. Dabalà, Large strain extrusion machining of magnesium alloys for biomedical applications, in: Procedia CIRP, 2018. doi:10.1016/j.procir.2018.05.080.

[95] Y. Liu, S. Cai, L. Dai, A new method for grain refinement in magnesium alloy: High speed extrusion machining, Mater. Sci. Eng. A. (2016). doi:10.1016/j.msea.2015.11.046.

[96] D. Sagapuram, M. Efe, K.P. Trumble, S. Chandrasekar, Flow transitions and flow localization in large-strain deformation of magnesium alloy, Mater. Sci. Eng. A. (2016). doi:10.1016/j.msea.2016.02.054.

[97] B. Song, R. Xin, G. Chen, X. Zhang, Q. Liu, Improving tensile and compressive properties of magnesium alloy plates by pre-cold rolling, Scr. Mater. 66 (2012) 1061–1064. doi:10.1016/j.scriptamat.2012.02.047.

[98] L. Jiang, J.J. Jonas, R.K. Mishra, A.A. Luo, A.K. Sachdev, S. Godet, Twinning and texture development in two Mg alloys subjected to loading along three different strain paths, Acta Mater. (2007). doi:10.1016/j.actamat.2007.03.006.

[99] M.R. Barnett, Z. Keshavarz, A.G. Beer, D. Atwell, Influence of grain size on the compressive deformation of wrought Mg-3Al-1Zn, Acta Mater. (2004). doi:10.1016/j.actamat.2004.07.015.

[100] M.D. Nave, M.R. Barnett, Microstructures and textures of pure magnesium deformed in plane-strain compression, Scr. Mater. 51 (2004) 881–885. doi:10.1016/j.scriptamat.2004.07.002.

[101] Y. Onuki, K. Hara, H. Utsunomiya, J.A. Szpunar, High-Speed Rolling of AZ31 Magnesium Alloy Having Different Initial Textures, J. Mater. Eng. Perform. 24 (2014) 972–985. doi:10.1007/s11665-014-1318-8.

[102] P. Yang, Y. Yu, L. Chen, W. Mao, Experimental determination and theoretical prediction of twin orientations in magnesium alloy AZ31, Scr. Mater. 50 (2004) 1163–1168. doi:10.1016/j.scriptamat.2004.01.013.

[103] E. Dogan, M.W. Vaughan, S.J. Wang, I. Karaman, G. Proust, Role of starting texture and deformation modes on low-temperature shear formability and shear localization of Mg-3Al-1Zn alloy, Acta Mater. 89 (2015) 408–422. doi:10.1016/j.actamat.2014.12.006.

[104] L.S. Tóth, A. Molinari, O. Bouaziz, Effective strain rate sensitivity of two phase materials, Mater. Sci. Eng. A. (2009). doi:10.1016/j.msea.2009.06.041.

[105] G.E. Dieter, H. a. Kuhn, S.L. Semiatin, Handbook of Workability and Process Design, 2003. doi:10.1361/hwpd2003p232.

[106] F. Kang, J.T. Wang, Y. Peng, Deformation and fracture during equal channel angular pressing of AZ31 magnesium alloy, Mater. Sci. Eng. A. (2008). doi:10.1016/j.msea.2007.09.063.